BNL-112413-2016-JA

Ligand-induced Dependence of Charge Transfer in Nanotube – Quantum Dot Heterostructures

Lei Wang, Jinkyu Han, Bryan Sundahl, Scott Thornton, Yuqi Zhu, Ruiping Zhou, Cherno Jaye, Haiqing Liu, Zhuo-Qun Li, Gordon T. Taylor, Daniel A. Fischer, Joerg Appenzeller, Robert J. Harrison, and Stanislaus S. Wong

Submitted to Nanoscale

July 2016

Condensed Matter Physics and Material Science Department

Brookhaven National Laboratory

U.S. Department of Energy
USDOE Office of Science (SC),
Basic Energy Sciences (BES) (SC-22)

DISCLAIMER

Ligand-induced Dependence of Charge Transfer in Nanotube – Quantum Dot Heterostructures

Lei Wang,[a] Jinkyu Han,[b] Bryan Sundahl,[c] Scott Thornton,[c] Yuqi Zhu,[d] Ruiping Zhou,[d]

Cherno Jaye,[e] Haiqing Liu,[a] Zhuo-Qun Li,[f] Gordon T. Taylor,[f] Daniel A. Fischer,[e]

Joerg Appenzeller,[d] Robert J. Harrison,[c,g] and Stanislaus S. Wong[a,b,*]

Email: stanislaus.wong@stonybrook.edu; sswong@bnl.gov

[a]Department of Chemistry, State University of New York at Stony Brook,

Stony Brook, NY 11794-3400

[b]Condensed Matter Physics and Materials Sciences Division,

Brookhaven National Laboratory, Building 480, Upton, NY 11973

[c]Institute of Advanced Computational Science, State University of New York at Stony Brook,

Stony Brook, NY 11794 USA

[d]Department of Electrical and Computer Engineering and Birck Nanotechnology Center,

Purdue University, West Lafayette, Indiana 47907

[e]Material Measurement Laboratory, National Institute of Standards and Technology,

Gaithersburg, Maryland 20889

[f]School of Marine and Atmospheric Sciences, State University of New York at Stony Brook,

Stony Brook, NY 11794-5000

[g]Computational Science Center, Brookhaven National Laboratory,

Upton, NY 11973 USA

Abstract

As a model system to probe ligand-dependent charge transfer in complex composite heterostructures, we fabricated double-walled carbon nanotube (DWNT) – CdSe quantum dot (QD) composites. Whereas the average diameter of the QDs probed was kept fixed at ~4.1 nm and the nanotubes analyzed were similarly oxidatively processed, by contrast, the ligands used to mediate the covalent attachment between the QDs and DWNTs were systematically varied to include *p*-phenylenediamine (PPD), 2-aminoethanethiol (AET), and 4-aminothiophenol (ATP). Herein, we have put forth a unique compilation of complementary data from experiment and theory, including results from transmission electron microscopy (TEM), near-edge X-ray absorption fine structure (NEXAFS) spectroscopy, Raman spectroscopy, electrical transport measurements, and theoretical modeling studies, in order to fundamentally assess the nature of the charge transfer between CdSe QDs and DWNTs, as a function of the structure of various, intervening bridging ligand molecules. Specifically, we correlated evidence of charge transfer as manifested by changes and shifts associated with NEXAFS intensities, Raman peak positions, and threshold voltages both *before* and *after* CdSe QD deposition onto the underlying DWNT surface. Importantly, for the first time ever in these types of nanoscale composite systems, we have sought to use theoretical modeling to justify and account for our experimental results. Our overall data suggest that (i) QD coverage density on the DWNTs varies, based upon the different ligand pendant groups used and that (ii) the presence of a π-conjugated carbon framework within the ligands themselves and the electron affinity of the pendant groups collectively play important roles in the resulting charge transfer from QDs to the underlying CNTs.

KEYWORDS: *NEXAFS, theoretical modeling, charge transfer, CdSe QDs, DWNTs, ligands*

Introduction

Semiconducting quantum dots (QDs) have been considered as candidate materials for the next generation of photovoltaic devices as a result of their unique attributes including (a) size-dependent opto-electronic properties, (b) a potential to maximize the production of hot photogenerated carriers through a multi-exciton generation effect, which would increase photoconversion efficiency, (c) a remarkable photostability, including resistance to photoinduced quenching, as well as (d) high extinction coefficients.[1] Double-walled carbon nanotubes (DWNTs), consisting of two coaxial tubules, represent a particularly interesting variation on the carbon-based anisotropic motif. By contrast with single-walled carbon nanotubes (SWNTs), in DWNTs, the outer shell of these structures can be selectively chemically functionalized while maintaining the physical integrity and hence, the favorable opto-electronic properties of the inner shell.[2-4] As such, DWNT - QD heterostructures, which merge the desirable properties of individual nanoscale constituent components into an integrated whole, embody a conceptually unusual architectural design in the field of photovoltaic cells.[5-8]

Typically, as-prepared QDs are capped with organic bulky long-chain, alkyl-based ligands, such as but not limited to trioctylphosphine oxide, tri-*n*-butylphosphine, oleylamine, hexadecylamine, and oleic acid. The presence of these molecular capping agents stabilizes QDs within a colloidal dispersion and allows for reproducible and precise control over QD size and by extension, the corresponding tuning of the QD bandgap.[9, 10] However, by their very structure, these unwieldy, bulky, and often non-conjugated ligands can effectively hamper charge transport and flow, which are inherently critical parameters to optimize for improving upon photovoltaic cell efficiency. Moreover, due to the insulating properties of these ligands, they often act as a

potential barrier to the charge transport capability between adjacent nanoparticles and nanostructures.[11, 12]

This issue can be potentially tackled by properly choosing electroactive ligand molecules and by performing the subsequent ligand exchange processes with the native ligands, in order to chemically modify and coat the external surfaces of these QDs with more conductive entities.[13] In this light, to tailor QDs for desirable photovoltaic behavior, a wide variety of ligands have been studied as candidates for potential capping agents of these nanoparticles, including bidentate aliphatic and aromatic thiols,[14] primary amines,[15] carboxylic acids,[16] and halide ions.[17] The judicious choice of ligands and the chemical modification of the outer surfaces of QDs through ligand exchange reactions are crucial for a number of reasons.

First, ligands can help to passivate surface defects, which play an important role in the surface-related emission and corresponding photostability of QDs. *Second*, on a relevant device level, the electronic properties of coupled colloidal QD solids can be precisely tuned through modification of the QD surface chemistry *via* ligand exchange, and such an approach designates a complementary strategy to control the QD bandgap through predictable variation of nanocrystal size.[18] *Third*, specific short bidentate ligands, such as ethanedithiol, not only reduce the interdot separation, thereby facilitating exciton dissociation and subsequent carrier transport towards the collecting contacts,[17, 19] but also serve as a molecular ligand bridge with which to connect QDs with other charge transporting components, such as the DWNTs herein, through either covalent or non-covalent attachment strategies.[20] Recently, our group has already shown that the synthesis of DWNT-CdSe QD heterostructures, using both covalent and non-covalent π-π conjugation protocols, mediated by specially chosen, short-chain ligands, 2-aminoethanethiol[21]

and 4-aminothiophenol,[22] is not only chemically feasible but also that there is a degree of charge transfer from the CdSe QDs to the DWNTs with the heterostructure itself.

Therefore, by deliberatively altering the identity of the ligands, we can vary the ligand length, the nature of the chemical binding groups, and the associated dipole moments, thereby leading to a shift in the positions of the QD valence band maximum and conduction band minimum. In doing so, we can potentially tune for efficient charge transfer, which is crucial to the development of QD-based photovoltaics.

With respect to previous and relevant studies on probing photo-induced charge transfer process in the CNT-QD systems, Weaver *et al.* reported on both electron and hole transfer from both CdSe QDs and the thiol-containing perylene compound (ETPTCDI) molecular linkers to the underlying CNTs, denoting processes which effectively increased the overall photon harvesting efficiency of the resulting nanocomposite.[23] In a separate work, based upon steady state and time resolved photoluminescence studies, rapid electron transport was observed between QDs and CNTs within ligand-free CdSe QD - CNT composites that had been fabricated using ultrasonication.[24] Additional examples abound. For example, Guo *et al.* designed graphene-CdSe QD composites bridged together by pyridine linkers, which not only enhanced the adhesion of QDs onto the graphene surface but also provided for good electronic coupling between the CdSe QDs and the underlying two-dimensional carbon allotrope, thereby leading to injection of *n*-type carriers within the graphene phase.[25]

Yet, although substantial research efforts have been expended with respect to analyzing charge transfer within CNT-QD composites, the precise role and function of the ligand molecules in this process is not entirely clear. To the best of our knowledge, there have been very few if any systematic efforts, involving either qualitative or quantitative studies, with the

objective of exploiting a cumulative combination of both experimental and theoretical techniques within the context of carbon nanotube (CNT)-QD systems to correlate the effect of varying ligand molecules with interfacial charge transfer in these nanocomposites.

Hence, in the current paper, our efforts are focused on gaining fundamental insights into charge transfer behavior across nanoscale interfaces within covalently bound DWNT-CdSe composite heterostructures as a function of the chemical nature of mediating ligand molecules, i.e. *p*-phenylenediamine (PPD), 2-aminoethanethiol (AET), and 4-aminothiophenol (ATP), respectively. The ligands we have purposely chosen to investigate intentionally probe the precise roles of both end group identity and physical structure. In fact, all other variables being equal, these ligands differ primarily either (i) in the identity of their terminal functional moiety or (ii) in the presence or absence of a conjugated π system.

The 3 ligand molecules we have analyzed are relatively short structures, with either a terminal –SH or $–NH_2$ group, possessing a strong affinity for Cd sites on the QD surface; the pendant $–NH_2$ group at the other end of the molecule can be potentially utilized to initiate possible amide formation with acid-functionalized CNTs in order to covalently generate the desired heterostructures. It is worth noting that these -SH or $–NH_2$ capped ligands are 'hole – scavengers'[26] and can act as effective acceptors for photogenerated holes.

Our group has previously reported on the presence of effective hole transfer from CdSe QDs to underlying DWNT networks, connected through ligands, i.e. using both the AET[27] and the ATP[22] ligands in separate studies. Nevertheless, despite the well-studied hole transfer behavior, electron transfer also exists in these types of systems, due to the band alignment of CdSe QDs with either adjacent DWNTs or metal oxides.[28, 29]

Therefore, in the current manuscript, the electron transfer processes in the DWNT-ligand-CdSe QD heterostructures will be probed through a unique combination of data acquired from complementary experimental techniques such as (i) transmission electron microscopy (*TEM*) images in order to nail down morphology and heterostructure formation as well as the corresponding QD coverage density within our various CNT-CdSe QD nanocomposites; (ii) near-edge X-ray absorption fine structure (*NEXAFS*) spectroscopy, which will provide information about the occupancy of the low-lying unoccupied electronic density of states, specific to the CdSe QDs and DWNTs;[30] (iii) *Raman* spectra of both constituent CNTs and the resulting heterostructures, with a focus towards analyzing and understanding relative changes in the positions and intensities of distinctive CNT-specific, Raman-active vibrational modes, which are sensitive to chemical doping;[31-34] and (iv) *electrical transport* measurements of heterostructures as manifested through the construction of field-effect transistor (FET) devices in order to monitor the effect of the 'doping' of DWNTs, induced by the presence of QDs. We emphasize that rarely if ever have all of these experimental techniques been collectively and advantageously used in a constructive, synergistic combination to analyze and to fundamentally understand the opto-electronic behavior of nanoscale composites of any composition.

As a unique corroboration for our insights, we have used theoretical X-ray absorption spectra (XAS) results, calculated based on Fermi's Golden Rule, to simulate, compare, and ultimately correlate computed results with measured NEXAFS experimental data in order to potentially test for and verify predictions from experiments. Although there are several papers that already deal with a comparison between DFT theoretical calculations and NEXAFS experimental data,[35-38] this current effort herein represents, to the best of our knowledge, the first attempt to comprehensively model a complex CNT-QD nanoscale heterostructure composite

system generated using various ligands, through the interpretation of (i) an ensemble of theoretical molecular modeling and DFT calculations, buttressed by (ii) a suite of microscopy and spectroscopy measurements in addition to (iii) device data. That is, we seek a holistic picture and understanding of linker-mediated charge interactions between the CdSe QDs and DWNTs.

Experimental

Materials.

DWNTs were purchased from Helix Material Solutions. In order to synthesize CdSe quantum dots, we started off with a number of molecular precursors including hexadecylamine (HDA) (90%), selenium powder (100 mesh, 99.5%), 1, 3-dicyclohexyl-carbodiimide (DCC) (99%), *p*-phenylenediamine (PPD) (99%), and 4-aminothiophenol (4-ATP) (97%), all of which were procured from Aldrich. In addition, we also purchased tri-*n*-octylphosphine oxide (TOPO) (99%), stearic acid (97%), cadmium oxide (CdO) (99%), tri-*n*-butylphosphine (TBP) (95%), and 2-aminoethanethiol hydrochloride (98%) (AET) from Acros Organics.

Synthesis.

Purification of DWNTs.

To remove the presence of metal particle catalysts and carbonaceous impurities, 50 mg of pristine DWNTs (Figure S1A†) were dispersed in 8 M diluted HNO_3 acid by sonication and then subsequent heating to 95°C for 20 h. The resulting purified and oxidized DWNTs (pDWNTs in Figure S1B†) were then filtered through a 200 nm polycarbonate membrane (Millipore), thoroughly washed with excess water, and finally dried at 80°C for 18 h.

Synthesis of CdSe QDs and ligand-exchange processes

To ensure consistency within the particle size distribution, batches of CdSe QDs possessing average diameters of 4.1 nm were prepared using a well-known and previously described protocol, with constant reaction times of ~100 s.[39] UV-visible and photoluminescence spectra (Figure S2A†) confirmed the absorption and emission profiles of as-prepared CdSe QDs, maintaining sizes of 4.1 nm. Powder X-ray diffraction data (Figure S2B†) were in agreement with a würtzite crystal structure of our QDs. In addition, the ligand exchange process was carried out on our as-prepared CdSe QDs in order to substitute the native TOPO and HDA capping agents with a targeted series of specific ligand moieties of interest.

In a typical experiment, 0.1 mmol of each ligand was dissolved in 2 mL methanol and added drop-wise to a suspension of as-prepared, TOPO/HDA-capped CdSe QDs (0.04 mmol) in 4 mL of hexane ([ligands]/[QDs] = 25). Under 'dark' conditions, individual methanolic mixtures of thiol-based AET and ATP ligands were stirred for 30 min; the analogous methanolic solution of PPD was heated at 40°C and stirred for 6 h under argon atmosphere, until the CdSe QDs could be subsequently precipitated, upon completion of the ligand exchange process.

As-generated ligand-exchanged QDs were then collected by centrifugation and subsequently washed with methanol and ethanol at 9000 rpm for 5 min for three successive times. The resulting processed QDs were ultimately re-dispersed in dimethyl sulfoxide (DMSO) for additional characterization. In order to confirm the presence of various ligand moieties bound onto the CdSe surface, a series of FT-IR spectra were collected and studied, as per the Supporting Information section (Figure S3†).

Synthesis of DWNT - PPD / AET / ATP-capped CdSe heterostructures by covalent attachment.

In a representative run, 1 mg of pDWNTs were dispersed in 10 mL DMSO by sonication followed by the addition of 35 mg of N,N'-dicyclohexylcarbodiimide (DCC) in

dimethylformamide (DMF) solution, a biochemically inspired protocol allowing for the activation of the surface carboxylic acid groups on the exterior of the pDWNTs and thereby facilitating the subsequent and effective immobilization of larger amounts of QDs anchored onto the DWNT surface in as little as 4 h of overall reaction time through the mediation of an amide bond. We note that we added 1-hydroxybenzotriazole (HOBT) to DCC in a molar ratio of 1: 1 in order to minimize the formation of an unwanted side product, e.g. diisopropylurea (DIU). A solution of 2 mL PPD/AET/ATP-capped CdSe QDs (0.004 mmol) in DMSO was subsequently introduced to the resulting solution and stirred in the 'dark' for 4 h. Upon reaction completion, the solution was filtered using 200 nm polycarbonate membranes (Millipore), extensively washed with distilled water and ethanol in order to remove excess free-standing CdSe QDs, and ultimately stored at 4°C, prior to further analysis.

Scheme 1 highlights a plausible reaction scheme associated with the synthesis of our DWNT-QD heterostructures, using a covalent attachment strategy. It is also worth mentioning that the creation of an amide bond (indicated in black) may not necessarily be the only bonding interaction that results in the attachment of QDs onto underlying DWNTs. Specifically, some QDs may additionally interact with the presence of oxygenated defects localized on the outer DWNT surface through the plausible mediation of a Cd-O-C linkage (highlighted as red dotted lines), due to the relatively favorable affinity for metal-oxygen bond formation.

Experimental and Theoretical Characterization.

Samples were thoroughly characterized using a number of different complementary structural methodologies, including transmission electron microscopy (TEM), Fourier transform infrared spectroscopy (FT-IR), Raman spectroscopy, and powder X-ray diffraction (XRD).

These data were complemented with additional opto-electronic data derived from UV-visible (UV-visible), photoluminescence, and near-edge X-ray absorption fine structure (NEXAFS) spectroscopies, supplemented by theoretical modeling results. We ultimately strengthened our interpretation with subsequent electrical transport measurements on field-effect transistors (FETs), generated from the resulting DWNT-QD heterostructures.

Electron Microscopy. Low-magnification TEM images were acquired at an accelerating voltage of 120 kV on a JEOL JEM-1400 instrument, equipped with a 2048 x 2048 Gatan CCD digital camera. Additional high-resolution TEM (HR-TEM) images were obtained using a JEOL JEM-2100F microscope, operating at an accelerating voltage of 200 kV outfitted with a Gatan Tridiem energy imaging filter. Specimens for all of these TEM runs were prepared by dispersing as-prepared samples in ethanol, sonicating for 2 min in order to ensure adequate dispersion, and finally depositing a drop of solution onto a 300 mesh Cu grid, coated with a lacey carbon film.

X-ray Diffraction. We characterized the crystallinity and crystallographic profile of our variously processed CdSe QDs using powder XRD. To analyze these materials, as-prepared samples were sonicated, dispersed in ethanol for about 2 min, and after deposition, finally air-dried onto transparent glass slides. Diffraction patterns for all of these materials were recorded using a Scintag diffractometer, operating in the Bragg configuration with Cu Kα radiation (λ = 1.54 Å) and scanning in the range from 20 to 80° at a rate of 0.25° per minute.

UV-visible spectra. UV-visible spectra were gathered at high resolution by using a Thermospectronics UV1 on sample dispersions within quartz cells, maintaining a 10 mm path length. Specifically, as-prepared QDs were suspended in hexane, and collected data were corrected in order to account for and subtract away the presence of the solvent background.

Photoluminescence spectra. As-prepared QDs were dispersed in hexane and sonicated

for 2 min, so as to produce a homogeneous dispersion. Relevant photoluminescence data were subsequently acquired at an excitation wavelength of 460 nm using a FluoroMax-4 spectrofluorimeter (Jobin Yvon).

FT-IR spectra. To obtain FT-mid-IR data on solid samples, we used a Nexus 670 (Thermo Nicolet) spectrometer, equipped with a single-reflectance zinc selenide (ZnSe) ATR accessory, a KBr beam splitter, and a DTGS KBr detector. A series of as-prepared, PPD-, AET-, and ATP-capped CdSe QD samples was then dried in a vacuum oven, prior to measurement. Solid samples were physisorbed onto a ZnSe crystal. Measurements were then taken in reflectance mode by using the Smart Orbit module.

NEXAFS. We were able to perform carbon *K*-, oxygen *K*-, and cadmium M_3-edge NEXAFS measurements at the NIST U7A beamline at the National Synchrotron Light Source located at Brookhaven National Laboratory. Specifically, NEXAFS spectra were achieved by using a horizontally polarized X-ray beam incident at 55^{o} (i.e. magic angle) and a channeltron electron multiplier equipped with a variable entrance grid bias. For the various elements studied, the entrance grid bias was set to –150 V in order to enhance surface sensitivity and to reduce the low-energy electron background. A toroidal spherical grating monochromator, comprised of a 600 lines/mm grating for the C *K*-edge data as well as a 1200 lines/mm grating for the Cd M_3 & O *K*-edges, was used. Slit openings of 30 μm × 30 μm along the beamline provided for an energy resolution of ~0.1 eV for all measured spectra. An electron flood gun set at 60 μA was used to mitigate for the possibility of surface charging.

The partial electron yield (PEY) signals were normalized to the incident beam intensity using the photoemission signal from a freshly evaporated Au mesh located along the incident beam path. The spectra were calibrated in terms of energy by analyzing the photoemission

current from an amorphous carbon mesh also located along the path of the incident beam. Spectra were calibrated and normalized using standard routines from the Athena software.[40]

Raman. Raman spectra were accumulated from our samples using a Renishaw inVia high resolution confocal Raman microscope that had been outfitted with a Leica DM2500 upright microscope using a 514.5 nm (2.41 eV) in line laser. The microscope stage was equipped with an automated *xyz*-motorized stage. Wavelength and intensity calibrations were completed by using an internal silicon standard, based upon a reference peak at 520 cm^{-1}.

Spectra from the samples were acquired using an 1800 line/mm grating, resulting in a spectral resolution of ~0.5 cm^{-1}, with a 10 s integration time per spectrum using a CCD array. Raw spectra were subsequently processed and analyzed using the WiRE 4.1 software. Baselines were subtracted from all of the spectra, and the integrated spectral areas were normalized to an area of 1. The resulting peaks were then fitted with 4 Lorentzian curves in order to determine the requisite peak positions, integrated areas (intensity), and peak widths.

Theoretical Modeling. Since the DWNTs used in our experiments possess outer diameters of about 10 nm and have tendency to form larger bundles, curvature and reduced dimension effects should be quite small, and thus, the outer surface of the DWNTs can be approximated by graphene in our theoretical modeling endeavors.[24] A finite model with a 3 nm square (410 carbon atoms) sheet of graphene was employed for the analysis. Electronic ground state calculations for the various complexes were computed using the NWChem[41] version 6.3, and specifically, the self-consistent density functional theory (DFT) calculations were achieved using the PBE-0 functional[42, 43] within the 6-31G*[44] basis set. Full details associated with the construction of the differentially functionalized systems as well as the sets of Cartesian coordinates used to describe them can be found in the Supporting Information.

Since relaxed core-hole calculations were too expensive on these systems with so many distinctive carbon atoms present, the theoretical X-ray absorption spectra (XAS) were calculated, according to Fermi's Golden Rule, using the dipole approximation as well as using unrelaxed orbitals and energies, following established practices.[45] Gaussian numerical broadening was used with a half width of 0.1 eV to model beam width and finite temperature effects. Since the core energies are not accurately predicted by DFT, theoretical spectra when compared with their experimental counterparts were shifted in order to align the large peak, attributed to the σ* transition. When comparing theory to theory, no shift was deemed to be necessary.

In a complex system characterized by a large population of polydisperse nanotubes, unforeseen numbers and types of defects and binding sites, as well as differential amounts of ligands and QD coverages, generating precise quantitative agreement with experimental results may be an unreasonable expectation. Nevertheless, herein we have employed standard, widely accepted methods in our analysis to acquire a basic, well-grounded qualitative understanding of the experimental behavior. In so doing, we have attempted to make sense of and to potentially de-convolute the acquired experimental results by systematically and separately identifying the independent contributions of the defects, the ligands, and the quantum dots, respectively. Details regarding the construction of the various model systems as well as a representative image of a typical graphene-ATP-CdSe QD composite, which is illustrative of our approach and captured in Vesta,[46] are displayed in Figure S4†.

Electrical Transport. CNT transistors have been fabricated onto 90 nm SiO_2/Si substrates. Specifically, CNTs have been deposited onto the substrate by drop coating and spinning until the solvent has been evaporated. To ensure that proper contacts with individual DWNTs could be achieved, a self-aligned e-beam writing procedure was employed, i.e. scanning

electron micrograph (SEM) images were taken after deposition of CNTs to identify their position relative to predefined alignment markers. Individual e-beam patterns were designed to contact CNTs both in the presence of and absence of ligand-capped CdSe QD decoration. After e-beam writing, source/drain metal contacts Ti/Au (30 nm / 30 nm) were deposited by the e-beam evaporator followed by a lift-off process. In our layout, the substrate has been used as the backgate in order to alter the local electrostatic conditions, and in particular, the injection conditions for carriers as a function of gate voltage, V_{gs}. Electrical measurements were performed using a probe station connected to a Hewlett Packard (HP) semiconductor parameter analyzer. In total, about 160 devices have been fabricated and measured. To reduce hysteresis, a pulse measurement method was applied, as described in a previous paper,[47] while the sample was kept under vacuum at 10^{-5} Torr.

Results and Discussion

We have chosen to organize our discussion on the key scientific issue of how systematically varying QD ligands alters charge transfer within composite nanoscale motifs through the 'prism' of particular data sets obtained from various complementary characterization techniques. Nonetheless, it is worth pointing out that to specifically deduce the effect of ligand identity, i.e. with all other parameters kept constant to ensure consistency, DWNT-CdSe heterostructures incorporating QDs with average diameters of ~4.1 nm *only* were generated by a covalent attachment strategy through the mediation of intervening PPD, AET, and ATP ligand molecules, respectively (Scheme 1).

TEM.

Low magnification TEM data in Figure 1 depicted the formation of all three, as-prepared heterostructures. The corresponding average coverage density on the underlying DWNT surface was noted to be 40 ± 12 dots for PPD-QDs, possessing an average diameter of 4.1 ± 0.9 nm (Figure 1A); 450 ± 55 dots for AET-QDs, maintaining average diameters of 4.1 ± 0.7 nm (Figure 1B); and 430 ± 30 dots with ATP-QDs, associated with average diameters of 3.9 ± 0.5 nm (Figure 1C), respectively. The DWNTs used to calculate the coverage density measured 500 nm in length and 30 nm in diameter (area: $1.5 \cdot 10^4$ nm^2) for a typical 'rectangular' bundle.

The use of 4.1 nm average diameter, AET and ATP-capped CdSe QDs resulted in substantially larger quantities of QDs attached onto the underlying DWNT surfaces (i.e. about 10 times as much as compared with their PPD analogues). Moreover, we noted a far more uniform nanoparticle coverage for these specific functionalized QDs on the sidewalls of the DWNT bundles as compared with heterostructures synthesized using PPD-CdSe QDs. These collective observations can be explained by the fact that the –SH group associated with the AET and ATP ligands possesses a stronger affinity for the CdSe QD surface by contrast with the $-NH_2$ group, thereby resulting in a greater coverage of these thiol-based ligands and consequently a higher probability and accessibility for QDs to be attached onto the DWNT surface frameworks.[48, 49]

The measured *d*-spacings of 3.52 Å and 3.41 Å in Figure 1 D-F could be ascribed to the *d*-spacing of the (002) lattice plane of the hexagonal phase of CdSe as well as to the interlayer spacing of the graphitic layer within DWNTs, respectively. One other feature worthy of note is that AET-QDs (Figure 1E) appear to have a larger tendency to aggregate as compared with their PPD-QD (Figure 1D) and ATP-QD (Figure 1F) counterparts, a finding which could possibly be ascribed to the shorter interdot distance as a result of the shorter ligand length associated with AET. To further confirm this observation, TEM and HRTEM images of various ligand-capped

CdSe QDs have been provided in Figure S5†. We confirm that the AET-QDs, highlighted by the yellow circles, tend to be more clustered, as compared with their other two derivatized analogues.

NEXAFS Spectra.

The C *K*-edge and O *K*-edge spectra of the pristine and oxidized DWNTs (Figures S6A and B†) were suggestive of the intrinsic success with the acid treatment of the DWNTs, by which oxygenated functionalities, e.g. –COOH groups, were generated on their external surfaces (see detailed analysis in the Supporting Information). Figures 2 highlighted the corresponding C and O *K*-edges as well as the Cd M_3-edge associated with the DWNT-PPD/AET/ATP capped-CdSe QD heterostructures. By means of comparison, all of the data associated with the various edges within the three ligand systems tested have been plotted on the same scale.

C *K*-edge. In principle, the C *K*-edge spectra correspond to the dipole transitions from C 1s core states to 2p-derived electronic states. The sharp peak at around 285.4 eV can be ascribed to a C 1s to the C=C 2p π* transition. The broad peak at 292-294 eV can be assigned to a convolution of three C 1s to C-C σ* transitions.[50, 51] In addition, the peaks at ~288.1 eV and ~289.1 eV can be attributed to the π* C=O and σ* C-O functionalities, respectively.[30, 52] Moreover, the areas under resonance (or peak intensity) of the various π* and σ* features are approximately proportional to the extent of the electronic density of the unoccupied C 2p derived states. Hence, the increased intensities of these features can be correlated either with the increased numbers of unoccupied C 2p states or with a charge transfer process taking place between the C 2p orbital of the nanotube and the immobilized 'dopant' species (such as Fe, Fe_3O_4, and SnO_2 specifically described in prior reports, for example)[51, 53, 54] at the interface.

Experimentally, when the ligands are attached onto the oxidized DWNTs (i.e. red spectra), the C *K*-edge (Figure 2A, D, and G) C=C π* transition intensity was found to be enhanced in the AET and ATP systems (black spectra), while no obvious change was observed for the PPD system. The reason for this enhancement will be discussed in the theory section.

After the QD deposition (i.e. blue spectra), we note that in all three of these heterostructures, the C *K*-edge π* transition intensity is either barely affected or perceptibly reduced in magnitude, whereas the σ * C-O transition evinced an enhanced intensity and a narrower peak as compared with the DWNT-PPD / AET / ATP nanoscale hybrid control sample prior to CdSe QD deposition (i.e. red spectra). These data suggest that the CdSe QDs donate charge onto the DWNT C=C π* states, while the sp^3 carbons in the σ* C-O states on the DWNTs may also back donate some charges to the CdSe QDs, possibly through the formation of a C-O-Cd link.[51, 55] One hypothesis consistent with our theoretical analysis is that the conjugated π* carbons are accepting electrons from the QDs, thereby resulting in a decrease in the unoccupied electronic density of states and giving rise to a suppressed signal, associated with the C=C π* transitions. By contrast, the σ* carbons associated with the oxygenated species are donating charges to the QDs, thereby causing an increase in the unoccupied electronic density of states and hence, an enhanced peak.

Nevertheless, we assert, based upon the strength of our cumulative data, that the amount of charge transfer from DWNTs to CdSe QDs is expected to be negligible as compared with charge transfer in the reverse direction from CdSe QDs to DWNTs, within the CdSe QD – DWNT heterostructures. We hypothesize that the slight increase in the π* C=O band intensity observed with AET-capped QDs may also denote possible evidence for electron transfer from the π* carbons within the C=O groups associated with the oxygenated species localized on the

surfaces of the DWNTs to the QDs, because the absence of a conjugated aromatic system inherent to the attached AET ligand itself renders a small, albeit finite, probability for this particular 'back donation' scenario. The broad σ* C-O peak (present in the oxidized and ligand-attached DWNTs) may be ascribed to the presence of σ conjugated structures of varying sizes, i.e. a superposition of σ* resonances. Upon addition of (interaction with) the QDs, some of these structures are chemically eliminated, thereby resulting in the narrowing of the peak.

Cd *M_3*-edge. In principle, the Cd M_3-edge is associated with transitions between the Cd 3p initial state and the unoccupied 5s states, which comprise the bottom of the conduction band of CdSe, based on the projected electronic density of states (DOS) proposed by theory. Hence, if the bottom of the CdSe conduction band were to shift by an energy interval, ΔE_c, then the corresponding M_3 absorption edge would shift by an equivalent amount, thereby representing the quantum confinement induced shift in the conduction band.[56, 57] The *M*-edges are known to suffer from weak signals and a large background[56] by contrast with the Cd L_3-edge. Therefore, in order to render these M_3-edges useful for quantitative analysis, multiple replicates of the spectra were collected with increased data integration times in order to obtain higher signal-to-noise ratios and therefore data interpretability.

Experimentally, within the heterostructure data set, the enhanced intensity of the Cd M_3-edge (Figure 2B, E, and H) provides direct evidence for charges being withdrawn from CdSe QDs upon deposition onto the DWNTs. Moreover, the heterostructures incorporating AET-QDs appeared to give rise to the largest enhancements observed, as noted by the drastic changes in the Cd M_3 edge (Figure 2E), as compared with their aromatic PPD and ATP analogues. This situation may possibly be ascribed to the shorter lengths of the aliphatic ligands, thereby resulting in a more extensive and favorable intermolecular charge transfer as compared with that

of analogous bulkier aromatic ligands.[58] Another viable contributive factor is the electron affinity of –SH, which has been calculated to be 2.23 and significantly, is higher in magnitude than that of -NH_2, i.e. 0.71.[59] The implication is that ligands with pendant thiol groups can potentially withdraw more charge from CdSe QDs as compared with their amine-terminating analogues.

Furthermore, it is also worth recalling from the TEM data (Figure 1) that the AET-based heterostructure possesses a higher coverage density (about 10 times) as compared with its PPD counterpart, a situation which might contribute to a larger amount of the observed charge transfer. Hence, because the Cd *M* edge spectra of each linker (2B, E and H) are pre-to-post edge normalized (to unity), on an atom-by-atom basis, we emphasize that the greatest enhancement of the Cd M_3-edge is detected with the AET-based heterostructure, an observation implying that the highest amount of charge transfer ascribed to the CdSe QDs is associated with the AET-capped CdSe QD system. To gain additional insights into the precise effect of QD coverage density associated with various ligands upon the resulting charge transfer, we have collected and interpreted complementary electrical transport measurements in Section 2.5.

O *K*-edge. In terms of the O *K*-edge, the two well-separated absorption features observed can be ascribed to a sharp peak located at 531.8 eV and a broader peak centered at around 539−546 eV. Specifically, the feature at ~531 eV can be potentially assigned to transitions from the O 1s core levels to the π* C=O states derived from carboxylic acid moieties, whereas the broad absorption feature centered at around 539−546 eV can possibly be attributed to the superposition of transitions arising from the O 1s core levels to the final states possessing σ* symmetry, localized on the O−H and C−O bonds. The small peak centered at ~534.6 eV likely derives from the -OH π* transition associated with carboxylic acid species.[60-62]

Experimentally, the π* -OH (534.6 eV) transition in the O *K*-edges (Figure 2C, F, and I) originating from carboxylic groups on the DWNT surface diminishes in all three of the heterostructures tested, suggestive of the formation of an amide bond upon QD deposition. Significant increases in both the π* and σ * transitions associated with the O *K*-edge spectra were also observed in all three of the heterostructures analyzed (i.e. blue spectra) as compared with the oxidized DWNT controls (i.e. red spectra), a likely consequence of electrons being withdrawn from the oxygen atoms ascribed to the oxygenated functional moieties on the DWNTs after chemical attachment of the adjoining QDs.

From all of the NEXAFS results associated with the C *K*-edge, O *K*-edge, and Cd M_3-edge data, it is reasonable to assert that charge is being transferred from CdSe (i.e. enhanced Cd M_3-edge intensity) to the C=C conjugated network of the ligand-functionalized DWNTs (i.e. a corresponding reduction in the C *K*-edge π* C=C transition intensity). In addition, the oxygen atoms associated with the surface oxidized C-O functionalities (such as carboxylic acid moieties on the oxygenated DWNT surface) are donating charge to the CdSe QDs and to the underlying DWNTs (i.e. as evidenced by an increase in the O *K*-edge π* C=O and σ* C-O transition intensities). We also expect a minor degree of charge back donation from carbons within the DWNTs to QDs, as manifested by alterations in the σ* C-O bond transitions (i.e. an enhanced C *K*-edge σ* C-O intensity after QD deposition).

It is also noteworthy that although the AET system demonstrates the largest enhancement in the Cd M_3-edge data, in the corresponding C *K*-edge spectra, the ATP system appears to have evinced the largest suppression (i.e. ~1 a.u. reduction) in the π* C=C transition (Figure 2G). We observed analogous albeit smaller intensity suppressions in the π* C=C transition with the PPD (i.e. ~0.5 a.u. diminution) and the AET-based (i.e. ~0.4 a.u. decrease) systems, respectively.

Nevertheless, what is intriguing about this data is that although there is a substantial discrepancy in the amount of QD coverage associated with heterostructures pertaining to the AET and PPD linkers, respectively, we actually observed very similar suppression behavior with only minor differences in the π* C=C transition for both composites, an observation which merits further investigation. That is, the C *K*-edge data would seem to suggest that the largest amount of charge transferred *from* the QDs to the underlying DWNTs occurs within the ATP-based heterostructures. Therefore, in order to further probe the effect of the intrinsic properties of each ligand upon the individual charge transfer processes observed, to normalize for the effect of QD coverage density, and to reveal more detailed insight into the charge transfer process from the QDs to the DWNTs as manifested by changes in the experimental C *K*-edge data, theoretical calculations of the C *K*-edge NEXAFS spectra have been performed on these various ligand systems, possessing identical QD coverage.

Theoretical Modeling.

In the theoretical models (see Experimental Section for full details), a flat graphene sheet measuring 3 nm x 3 nm, with 20 carboxyl group defects randomly spaced around the interior of the sheet, was created. The presence of the linker molecules was subsequently built into this 'defected' system, with the ligand molecules attached at the same 'defected' sites in the graphene sheet. QDs possessing a relaxed geometry of 1.3 nm were subsequently attached onto the ligand-capped graphene. Figure 3 overlays the experimental (purple) with theoretical (green) C *K*-edge NEXAFS spectra of various linker-modified graphene species (Figure 3A, C and E) as well as of the corresponding linker-derivatized graphene-CdSe QD heterostructures (Figure 3B, D and F), with theory shifted to align with the experimental σ* peak located at 293 eV. Both data sets have

been normalized, such that the σ* peak located at 293 eV has a spectral intensity of 1. A comparison highlights the overall agreement in terms of the relative positions and intensities of the π^* and σ* peaks associated with the various species. The calculated C *K*-edge spectra of pristine graphene (red), of defect-ridden (oxidized) graphene (blue), of various ligand species bound to graphene (green), as well as of heterostructures characterized by CdSe QDs attached to various ligand-modified graphene species (purple) are displayed in Figure 4.

Before QD deposition (ligand bound to graphene systems). As previously mentioned, with respect to the experimental NEXAFS data connected with ATP-bound DWNTs (i.e. red curve in Figure 2G), the C=C π^*(~279 eV) intensity appears to be noticeably enhanced relative to that of oxidized graphene alone (i.e. black curve in Figure 2G). A measurable enhancement was observed as well with the simulated spectra for the calculated ATP-bound graphene (i.e. green curve in Figure 4C) as compared with the signal for oxidized graphene alone (i.e. blue curve in Figure 4C).

By contrast, the calculated AET-bound graphene did not give rise to a significant change in C *K*-edge behavior as compared with that of the oxidized graphene alone (i.e. blue curve as compared with the green curve in Figure 4B). Moreover, it was noted that in both the experimental (Figure 2D) and theoretical systems (Figure 4B), the AET-bound graphene evinced appreciably less enhancement in C=C π^* intensity as compared with its ATP-linked analogue.

It is also worth mentioning that the enhancement is rather obvious with the calculated PPD-bound graphene system (i.e. green curve) as compared with oxidized graphene alone (i.e. blue curve in Figure 4A). However, such a scenario was not necessarily confirmed by the experimental NEXAFS data (i.e. red curve as compared with black in Figure 2A), and this

discrepancy might have been possibly ascribed to the much lower spatial coverage density of PPD ligands within the experimental PPD-bound DWNT system.

In order to further investigate this enhancement, Figure 5 delineates the contribution of the various constituent groups of carbons to the total spectrum associated with the PPD, AET, and ATP-bound graphene systems, including (1) the C=C backbone carbons within the graphene layer (i.e. the carbon atoms in the plane of the graphene sheet, labeled as the "sheet" carbon, herein) and (2) the carbon atoms associated with the ligands themselves (i.e. the carbon atoms out of the plane of the graphene, labeled as the "linker" carbon, herein).

It is apparent that the origin of the large increase in the C=C π^* peak near 279 eV for the PPD and ATP-bound graphene systems (i.e. green curves) as compared with oxidized graphene alone (i.e. blue curves) in Figure 4A and C) can be ascribed to the aromatic carbon atoms present within the ligands themselves, which constitute the major component of the total C=C π^* peak signal in Figure 5A and C. Such an enhancement in the experimental data associated with ATP-bound DWNTs (i.e. red curve) relative to that of the oxidized DWNTs itself (i.e. black curve) is also apparent in Figure 2G, but it is not as evident with the PPD-bound DWNT system in Figure 2A, an observation possibly due to the much lower coverage density of PPD within the experimental PPD-bound DWNT system. The corresponding lack of a large increase in the C=C π^* peak intensity near 279 eV for AET-bound graphene (i.e. green curve, Figure 4B) can be attributed to the fact AET does not possess aromatic carbons within the ligand itself (Figure 5B). Hence, the spectra for the AET, ATP, and PPD-bound graphene systems are very similar with respect to the carbon atoms within the sheet itself, with only a slight increase in the intensity of the peak located at 278 eV for the AET-bound graphene system (i.e. blue curve in Figure 5B).

After QD deposition (CdSe QDs chemically attached onto ligand-bound graphene systems). After CdSe QD deposition, a reduction of the C=C π^* transition was observed for the CdSe-ATP-graphene system as compared with ATP-graphene itself (i.e. purple curve as compared with green curve in the Figure 4C inset), denoting behavior which is consistent with the corresponding experimental data shown in Figure 2G (blue as compared with red curves). A smaller reduction was noted in the C=C π^* transition of the CdSe-PPD-graphene composite as compared with PPD-graphene itself (i.e. purple curve as compared with green curve in the Figure 4A inset). Only a marginal diminution was observed with the CdSe-AET-graphene heterostructure as compared with AET-graphene itself (i.e. purple curve as compared with green curve in the Figure 4B inset).

While theory was able to correctly predict the relevant qualitative trends, it is also worth pointing out at the outset that the precise quantitative amount of intensity suppression within the experimental NEXAFS spectra data was not fully reflected in the corresponding theoretically simulated analogues. This reality might be indicative of the fact that the model used may have been insufficient to accurately capture the entirety of the charge transfer phenomena in play, possibly due to the smaller size of the QD used in the model simulations (i.e. 1.3 nm for ease and interpretability of calculation as compared with 4.1 nm in the actual experiments).

In particular with the CdSe-ATP-graphene heterostructures, the total decrease in the C=C π^* peak intensity appears to be much larger than what has observed for both the AET and PPD-based analogues. In order to further investigate the suppression in the C=C π^* transition after QD deposition, the various 'differential' carbon contributions to the simulated C *K*-edge NEXAFS spectra associated with the CdSe QD-ligand-graphene heterostructures as compared with the analogous ligand-bound graphene system are highlighted in Figure 6.

The largest suppression was noted with the CdSe-ATP-graphene system after the QD deposition (i.e. purple curve) as compared with ATP-graphene itself (i.e. green curve in Figure 6G and Figure 4C inset). In effect, the ligand carbons (Figure 6H) contribute to the largest reduction in the π^* peak amongst all three of the ligand systems tested. We have also observed that the C=C π^* peak associated with the "sheet" carbon atoms (Figure 6I) remain relatively unchanged when the QD is added. The smallest reduction was actually observed in the C=C π^* peak near 279 eV for the CdSe-AET-graphene system (i.e. purple curve) as compared with AET-graphene itself (i.e. green curve in Figure 6D and Figure 4B inset). This decrease can be attributed to the carbon atoms within the graphene sheet, likely experiencing suppression in their intensity at this energy level (Figure 6F). There is a corresponding noticeable enhancement of the peak attributed to the "ligand" carbons at 282 eV (Figure 6E), which is consistent with experimental data presented in Figure 2D.

For the graphene carbon atoms in the CdSe-PPD-graphene system (i.e. purple curve), a reduction is noted in the π^* peak intensity as compared with the analogous PPD-graphene system (i.e. green curve in Figure 6A and Figure 4A inset)**.** This decrease can be attributed to the sp^2 carbons within the ligand (Figure 6B). The first thing to note is that the addition of QDs can reduce the intensity of nearly all energies, with the only exceptions being around 281 and 282 eV, associated with the σ* C-O functionalities, which yielded a small amount of enhancement from the carbon atoms in the graphene sheet and the ligand region (Figure 6B and C). The suppression of nearly every peak and the corresponding enhancement of the peak at 282 eV in the CdSe-PPD-graphene system are consistent with experiment (Figure 2A). The locations of both calculated π^* and σ* peaks also correlate well with experiment (Figure 2A), though the intensity of the theoretical CdSe-PPD-graphene system was found to be different from what experiment

yielded. This latter discrepancy may be due to the higher coverage of the PPD ligands in the simulated system as compared with the corresponding coverage of the PPD ligands within the experimental CdSe-PPD-DWNT system.

Our calculated C *K*-edge NEXAFS spectra imply that when normalized to the same amount of QD coverage density, the CdSe-ATP-graphene heterostructure gave rise to the largest decrease in the C=C π^* peak. Successively lower reductions in the C=C π^* peak intensities were noted for the CdSe-graphene-PPD and AET-based systems, respectively, with the AET-associated composite yielding the least amount of π^* peak reduction.

Summation. To recapitulate, despite differences between theory and experiment in terms of ligand coverage and QD size, theory reproduces the overall experimental trends observed. With respect to the ligand-bound graphene systems, theory and experiment mutually confirm the presence of the largest enhancement in the C=C π^* peak of the ATP-derivatized graphene, and the least enrichment for the AET-functionalized graphene. Theory explains these trends on the basis that the sp^2 carbon atoms within the ATP ligand share a similar chemical environment with the carbon atoms of the graphene sheet and can therefore add onto the C=C π^* peak intensity directly, whereas the analogous sp^3 carbons within the AET ligand do not. Experimentally, the PPD ligands maintained such a low spatial coverage that this trend was not observed.

When analyzing the extent of the C=C π^* peak suppression occurring upon the addition of QDs, theory and experiment both were in agreement that use of the ATP ligand gave rise to the strongest decline, whereas the AET linker yielded significantly less peak intensity decrease. Indeed, theory explains the overall observed ‘suppression’ as arising primarily from a diminution in the intensity emanating from the carbons in the ligands themselves in the aromatic ligand systems. These data are consistent with the experimental results presented in Figure 2A and G,

and the calculated XAS shown in Figure 4A and C. This finding moreover corroborates previous published results which suggest that electron-rich, conjugated systems are more efficacious at enabling the charge transfer process as compared with their non-conjugated counterparts.[63]

Raman.

The Raman spectra associated with both pristine and oxidized DWNTs are presented in Figure S7†. Specifically, we find that the intensity ratio of the D band located at 1340 cm^{-1} to the tangential mode (G band) localized at 1580 cm^{-1} (I_D/I_G) definitively enhances after the purification process. We note that the increase in the I_D/I_G ratio due to the purification process is expected, since the augmented peak intensity associated with the D band can typically be attributed to expected damage and distortion of the intrinsic conjugated sp^2 carbon lattice, arising from the presence of amorphous carbon[64] and other symmetry-breaking defects in the DWNTs generated during the oxidation and concomitant surface functionalization of the outer surfaces of DWNTs. This DWNT purification/oxidation process is manifested in the formation of –COOH and other oxygenated species on the external surfaces of our tubes.[65, 66]

The tangential modes (G bands) typical of DWNT-PPD / AET / ATP-CdSe heterostructures together with the corresponding DWNT-PPD / AET / ATP control samples are highlighted in Figure 7A-C. Each individual G band was treated as a convolution of 4 Lorentzian functions (i.e. the dashed curves). The two peaks located at the higher frequencies can be attributed to the G^+ and G^- bands of the semiconducting outer tube, whereas the other two peaks associated with the lower frequencies correspond to the G^+ and G^- bands of the semiconducting inner tube. According to the Kataura plot,[67] the 2.41 eV excitation energy of the laser is in resonance with the E_{33}^S transition of a semiconducting (S) outer tube as well as with the E_{33}^S

transition of a semiconducting (S) inner tube. The fits of the sum of the Lorentzian peaks match well with previously reported G-band deconvolution data on DWNTs, possessing a S@S configuration.[68, 69] In particular, the peak located at higher frequency can be ascribed to the unresolved A_1 and E_1 tangential G^+ modes for the outer tubes.[70]

Upon deposition of CdSe QDs, all of the outer tube G^+ sub-bands evince an apparent peak down-shift and a corresponding intensity decrease, an observation which can be potentially attributed to the G-band 'softening', indicative of the expansion of C-C bonds upon *n*-type doping and suggestive of the presence of electron transfer *from* QDs to the DWNTs in all three of the ligand systems analyzed.[71, 72] ATP-based heterostructures gave rise to the largest down shift in the peak position recorded of 16 cm^{-1}, as compared with 2 cm^{-1} and 7 cm^{-1} associated with PPD and AET-based analogues, respectively. These data are consistent with complementary observations from both experimental and calculated NEXAFS data, indicating the largest amount of electron transfer with ATP-centric systems. Although the observed changes in the PPD and AET-based systems are reasonably comparable in terms of the measured peak downshift, as a result of the much higher coverage density of AET-CdSe QDs as compared with PPD-CdSe QDs within our heterostructures (Figure 1A and B), the use of aromatic PPD might actually be a more promising and efficient ligand choice in terms of promoting charge transfer.

Electrical Transport Measurements.

The combination of NEXAFS and Raman spectroscopy data has experimentally confirmed the presence of charge transfer between immobilized CdSe QDs and the underlying DWNTs. In order to further probe the potential device capabilities of our as-generated DWNT-CdSe QD heterostructures for photoelectronic applications, additional electrical transport

measurements of associated FETs have been acquired. When performing electrical transport measurements within a three-terminal FET geometry, critical information about the charge state of the pristine and ligand-QD decorated carbon nanotubes can be gathered from the gate voltage dependence of the respective devices.[73] It is worth mentioning here that all of the measurements have been carried out under 'dark' conditions, meaning the ligand-capped CdSe QDs themselves are not being excited. Hence, the observed charge-transfer behavior is not associated with photoinduced excitons, but rather with possible work function differences among the various individual components in the system.

All measurements were performed at room-temperature at a pressure of $\sim 1 \cdot 10^{-5}$ torr. Device characteristics obtained in this way are very similar in appearance (inset of Figure 8) but exhibit their current minima at distinctly different gate voltages, depending on the particular type of ligand analyzed (Figure 8). In fact, in these CNT devices, it is this unique fingerprint characterized by a shift in the threshold voltage (relative to V_{gs}) that holds information about the amount of charge transfer that can occur between the ligand-QD system and the attached DWNTs, due to their different work functions.

Figure 8 highlights the gate voltage at which the current through the device is minimum (V_{min}) with the relevant transfer characteristics obtained for four different types of samples: (a) pristine DWNTs; (b) DWNTs coupled with ~4.1 nm diameter AET-QDs; (c) DWNTs immobilized with ~4.1 nm diameter ATP-QDs; and (d) DWNTs connected to ~4.1 nm diameter PPD-QDs. To obtain a decent statistical distribution, about 40 devices were fabricated and measured for each functionalization type. Only devices showing clear ambipolar behavior, i.e. electron currents for positive gate voltages and hole currents for negative gate voltages, have been included in the analysis. Relative to pristine CNT FETs, all functionalized tube devices

show a clear negative shift of V_{min}, which indicates that electrons are being transferred from the ligand-QD system to the DWNTs. Indeed, the performance of the CNT FET devices is indicative of electron transfer both to and from DWNTs. Nevertheless, it is obvious that the electron transfer from QDs to DWNTs is the predominant effect as compared with possible electron back-donation from the DWNTs to the QDs, since the FET devices tested herein primarily substantiated and were consistent with the presence of an *n*-doping effect after QD decoration.

Figure 9 summarizes the distribution of V_{min} values for the various ligand-QD CNT devices as a function of the respective QD coverage densities on the underlying DWNTs, as extracted from TEM. To summarize, the data suggest that in the absence of laser illumination, the QD-ligand system once attached to the DWNT is no longer "charge neutral" and in fact, systems possessing higher QD coverage densities lead to more charge transfer to the DWNT (Table 1). Measurements of the various DWNT−ligand-capped CdSe QD heterostructures in the presence of laser illumination are still under investigation in order to reveal additional insights into photoinduced charge transport.

Conclusions

In this manuscript, various DWNT-CdSe heterostructures, with average QD diameter of 4.1 nm, have been successfully synthesized using a covalent attachment approach through the mediation of PPD, AET, and ATP ligands, respectively. To the best of our knowledge, we are the first to probe and correlate the specific scientific issue of *ligand* structure and chemistry upon measurable and observable physical properties in nanoscale heterostructures. Hence, with a collective analysis of both experimental and theoretical data sets uniquely applied to this

problem, plausible evidence for charge transfer has been proposed for heterostructures generated through the mediation of these various, specifically chosen ligands.

Focusing on the role of the *pendant functional group* within the ligand, TEM and HRTEM images have indicated that the PPD-capped CdSe QDs gave rise to a lower coverage density as compared with AET and ATP-based heterostructures, possibly due to the weaker binding strength of $–NH_2$ as compared with the –SH groups with respect to the Cd sites of the QD surface. Specifically, the larger experimental NEXAFS enhancement associated with the Cd *M_3-edge* transition intensity for the AET-based (versus PPD-bound) heterostructures was likely a consequence not only of their greater QD coverages but also of the higher electron affinity of the AET's terminal –SH groups as compared with PPD's pendant $–NH_2$ moieties. The net consequence was an overall increased charge withdrawal and charge transfer from the immobilized CdSe QDs within the AET-mediated heterostructures. Subsequent electrical transport measurements suggest that in the absence of laser illumination, the QD-ligand system once attached to the DWNT is no longer "charge neutral", and *systems possessing higher QD coverage densities lead to more charge transfer* to the underlying DWNTs.

Concentrating on the function of the carbon-rich *π-conjugated system* within the ligand structure, analysis of the experimental C *K*-edge spectra, specifically the C=C π* transition, as well as of the Raman spectra of the DWNT G^+-band down-shift have unambiguously suggested a more nuanced picture in which the ATP-based heterostructures actually gave rise to the largest amount of charge transfer observed from the QDs to the underlying DWNTs. We hypothesize that although both ligands similarly possess pendant –SH functional groups as well as similar QD coverage densities, the presence of the ATP's intrinsic π-conjugated aromatic system mediates and facilitates greater charge transfer as compared with its aliphatic AET counterpart.

Nonetheless, the aromatic PPD-based system yielded a smaller amount of charge transferred to DWNTs as compared with their aliphatic ATP-based analogues, possibly due to the much lower QD coverage density and concentrations, i.e. 1/10 for PPD versus ATP-based composites.

Our overall data point to the presence of the π-conjugated carbon system as well as the pendant groups within the ligands as important contributive factors governing the resulting charge transfer to the underlying CNTs. Theoretical NEXAFS data reproduced the overall experimental trends in terms of enhancement/suppression behavior of the C=C π* peak (Figure 3). In particular, the use of theory explained the origin of the C=C π* peak enhancement in the graphene-linker systems as arising from the nature of carbon atoms within the linker (Figure 5) and the suppression of the C=C π* peak is stronger within the conjugated systems (Figure 4). Theory could not conclusively ascribe the C=C π* peak suppression to the effect of charge transfer. However, it is crucial to note that whereas by virtue of creating a computationally tractable system, the theory calculations necessarily focused upon a QD with a relaxed geometry of 1.3 nm, experimental QDs were actually substantially larger (4 nm) and often aggregated, a scenario which would be expected to transfer more charge.

In other words, theory could effectively and qualitatively account for all of the observed phenomena and behavior at the smallest of dimensions. Our computationally-based insights therefore represent an excellent foundation upon which to more fully understand molecule-mediated optoelectronic behavior within nanoscale heterostructures in general. Hence, future efforts will explore the idea of scaling these size-dependent effects to macroscopic regimes involving larger-sized and greater numbers of quantum dots.

Acknowledgements

Research support for LW, JH, YZ, RZ, HL, JA, and SSW) was provided by the U.S. Department of Energy (DOE), Basic Energy Sciences, Materials Sciences and Engineering Division. NEXAFS experiments were carried out at the National Synchrotron Light Source at Brookhaven National Lab, which is supported by the U.S. DOE under Contract No. DE-SC-00112704. DFT results in this manuscript are based in part upon work performed at the Institute for Advanced Computational Science, SUNY Stony Brook with support from New York State and the IACS endowment fund. RJH also acknowledges support from the National Science Foundation (NSF) under award number ACI-1216644. Raman data were acquired at SBU's Nano-Raman Molecular Imaging Laboratory (NARMIL), established with NSF MRI grant OCE-1336724. Certain commercial names used herein are for illustrative purposes only, and do not constitute an endorsement by the National Institute of Standards and Technology.

Notes and References

1. G. H. Carey, A. L. Abdelhady, Z. Ning, S. M. Thon, O. M. Bakr and E. H. Sargent, *Chem. Rev.*, **2015**, **115**, 12732–12763.
2. Y. Tison, C. E. Giusca, V. Stolojan, Y. Hayashi and S. R. P. Silva, *Adv. Mater.*, 2008, **20**, 189-194.
3. A. Hashimoto, K. Suenaga, K. Urita, T. Shimada, T. Sugai, S. Bandow, H. Shinohara and S. Iijima, *Phys. Rev. Lett.*, 2005, **94**, 045504/1-4.
4. R. Saito, R. Matsuo, T. Kimura, G. Dresselhaus and M. S. Dresselhaus, *Chem. Phys. Lett.*, 2001, **348**, 187-193.
5. C. Schulz-Drost, V. Sgobba, C. Gerhards, S. Leubner, R. M. K. Calderon, A. Ruland and D. M. Guldi, *Angew. Chem., Int. Ed.*, 2010, **49**, 6425-6429.
6. D. F. Wang, J. K. Baral, H. G. Zhao, B. A. Gonfa, V. V. Truong, M. A. El Khakani, R. Izquierdo and D. L. Ma, *Adv. Funct. Mater.*, 2011, **21**, 4010-4018.
7. P. Reiss, M. Protiere and L. Li, *Small*, 2009, **5**, 154-168.
8. L. H. Zhang, E. Z. Shi, Z. Li, P. X. Li, Y. Jia, C. Y. Ji, J. Q. Wei, K. L. Wang, H. W. Zhu, D. H. Wu and A. Y. Cao, *Phys. Chem. Chem. Phys.*, 2012, **14**, 3583-3588.
9. W. W. Yu and X. Peng, *Angew. Chem., Int. Ed.*, 2002, **41**, 2368-2371.
10. Z. A. Peng and X. Peng, *J. Am. Chem. Soc.*, 2001, **123**, 183-184.
11. T. Virgili, I. S. López, B. Vercelli, G. Angella, G. Zotti, J. Cabanillas-Gonzalez, D. Granados, L. Luer, R. Wannemacher and F. Tassone, *J. Phys. Chem. C*, 2012, **116**, 16259-16263.
12. C. Querner, P. Reiss, S. Sadki, M. Zagorska and A. Pron, *Phys. Chem. Chem. Phys.*, 2005, **7**, 3204-3209.
13. J. C. Newton, K. Ramasamy, M. Mandal, G. K. Joshi, A. Kumbhar and R. Sardar, *J. Phys. Chem. C*, 2012, **116**, 4380-4389.
14. E. J. D. Klem, D. D. MacNeil, P. W. Cyr, L. Levina and E. H. Sargent, *Appl. Phys. Lett.*, 2007, **90**, 183113.
15. D. V. Talapin and C. B. Murray, *Science*, 2005, **310**, 86-89.
16. A. G. Pattantyus-Abraham, I. J. Kramer, A. R. Barkhouse, X. Wang, G. Konstantatos, R. Debnath, L. Levina, I. Raabe, M. K. Nazeeruddin, M. Gratzel and E. H. Sargent, *ACS Nano*, 2010, **4**, 3374-3380.
17. J. Tang, K. W. Kemp, S. Hoogland, K. S. Jeong, H. Liu, L. Levina, M. Furukawa, X. Wang, R. Debnath, D. Cha, K. W. Chou, A. Fischer, A. Amassian, J. B. Asbury and E. H. Sargent, *Nat. Mater.*, 2011, **10**, 765-771.
18. P. R. Brown, D. Kim, R. R. Lunt, N. Zhao, M. G. Bawendi, J. C. Grossman and V. Bulovic, *ACS Nano*, 2014, **8**, 5863-5872.
19. I. Mora-Sero, L. Bertoluzzi, V. Gonzalez-Pedro, S. Gimenez, F. Fabregat-Santiago, K. W. Kemp, E. H. Sargent and J. Bisquert, *Nat. Commun.*, 2013, **4**, 3272.
20. X. H. Peng and S. S. Wong, *Chem. Mater.*, 2009, **21**, 682-694.
21. X. Peng, M. Y. Sfeir, F. Zhang, J. A. Misewich and S. S. Wong, *J. Phys. Chem. C*, 2010, **114**, 8766-8733.
22. L. Wang, J. Han, J. Hoy, F. Hu, H. Liu, M. M. Gentleman, M. Y. Sfeir, J. A. Misewich and S. S. Wong, *Dalton Trans.*, 2014, **43**, 7480-7490.
23. J. E. Weaver, M. R. Dasari, A. Datar, S. Talapatra and P. Kohli, *ACS Nano*, 2010, **4**, 6883-6893.

24. S. Azoz, J. Jiang, G. Keskar, C. McEnally, A. Alkas, F. Ren, N. Marinkovic, G. L. Haller, S. Ismail-Beigi and L. D. Pfefferle, *Nanoscale*, 2013, **5**, 6893-6900.
25. S. R. Guo, D. D. Bao, S. Upadhyayula, W. Wang, A. B. Guvenc, J. R. Kyle, H. Hosseinibay, K. N. Bozhilov, V. I. Vullev, C. S. Ozkan and M. Ozkan, *Adv. Funct. Mater.*, 2013, **23**, 5199-5211.
26. I. S. Liu, H. H. Lo, C. T. Chien, Y. Y. Lin, C. W. Chen, Y. F. Chen, W. F. Su and S. C. Liou, *J. Mater. Chem.*, 2008, **18**, 675-682.
27. X. H. Peng, J. A. Misewich, S. S. Wong and M. Y. Sfeir, *Nano Lett.*, 2011, **11**, 4562-4568.
28. K. Yu, G. Lu, K. Chen, S. Mao, H. Kim and J. Chen, *Nanoscale*, 2012, **4**, 742-746.
29. I. Robel, B. A. Bunker and P. V. Kamat, *Adv. Mater.*, 2005, **17**, 2458-2463.
30. A. D. Winter, E. Larios, F. M. Alamgir, C. Jaye, D. A. Fischer, M. Omastova and E. M. Campo, *J. Phys. Chem. C*, 2014, **118**, 3733-3741.
31. G. M. do Nascimento, T. Hou, Y. A. Kim, H. Muramatsu, T. Hayashi, M. Endo, N. Akuzawa and M. S. Dresselhaus, *Nano Lett.*, 2008, **8**, 4168-4172.
32. G. M. do Nascimento, T. Hou, Y. A. Kim, H. Muramatsu, T. Hayashi, M. Endo, N. Akuzawa and M. S. Dresselhaus, *J. Phys. Chem. C*, 2009, **113**, 3934-3938.
33. J. Cambedouzou, J. L. Sauvajol, A. Rahmani, E. Flahaut, A. Peigney and C. Laurent, *Phys. Rev. B*, 2004, **69**, 235422.
34. G. M. do Nascimento, T. Hou, Y. A. Kim, H. Muramatsu, T. Hayashi, M. Endo, N. Akuzawa and M. S. Dresselhaus, *Carbon*, 2011, **49**, 3585-3596.
35. E. Warszawski, J. Adler, A. Hoffman and A. Silverman, *Proceedings of the 22th Workshop on Computer Simulation Studies in Condensed Matter Physics (CSP 2009)*, 2010, **3**, 1381-1385.
36. X. Qian, H. Sambe and D. E. Ramaker, *Phys.Rev. B*, 1995, **52**, 15115-15121.
37. E. Voloshina, R. Ovcharenko, A. Shulakov and Y. Dedkov, *J. Chem. Phys.*, 2013, **138**, 154706.
38. B. J. Schultz, C. Jaye, P. S. Lysaght, D. A. Fischer, D. Prendergast and S. Banerjee, *Chem. Sci.* 2013, **4**, 494-502.
39. L. H. Qu and X. G. Peng, *J. Am. Chem. Soc.*, 2002, **124**, 2049-2055.
40. B. Ravel and M. Newville, *J. Synchrotron Rad.*, 2005, **12**, 537-541.
41. M. Valiev, E. J. Bylaska, N. Govind, K. Kowalski, T. P. Straatsma, H. J. J. Van Dam, D. Wang, J. Nieplocha, E. Apra, T. L. Windus and W. A. de Jong, *Comput. Phys. Commun.*, 2010, **181**, 1477-1489.
42. M. Ernzerhof and G. E. Scuseria, *J. Chem. Phys.*, 1999, **110**, 5029-5036.
43. C. Adamo and V. Barone, *J. Chem. Phys.*, 1999, **110**, 6158-6170.
44. V. A. Rassolov, J. A. Pople, M. A. Ratner and T. L. Windus, *J. Chem. Phys.*, 1998, **109**, 1223-1229.
45. D. Prendergast and G. Galli, *Phys. Rev. Lett.*, 2006, **96**, 215502.
46. K. I. Momma, F., *J. Appl. Cryst.*, **2011**, ***44***, 1272-1276.
47. E. David, D. Sumit, L. Albert and P. Eric, *Nanotechnology*, 2010, **21**, 085702.
48. A. M. Munro, I. Jen-La Plante, M. S. Ng and D. S. Ginger, *J. Phys. Chem. C*, 2007, **111**, 6220-6227.
49. C. Park and T. Yoon, *Toxicology and Environmental Health Sciences*, 2009, **1**, 151-158.
50. C. Liu, S. Lee, D. Su, Z. Zhang, L. Pfefferle and G. L. Haller, *J. Phys. Chem. C*, 2012, **116**, 21742-21752.

51. Z. Wang, L. Wu, J. Zhou, W. Cai, B. Shen and Z. Jiang, *J. Phys. Chem. C*, 2013, **117**, 5446-5452.
52. A. Kuznetsova, I. Popova, J. T. Yates, M. J. Bronikowski, C. B. Huffman, J. Liu, R. E. Smalley, H. H. Hwu and J. G. G. Chen, *J. Am. Chem. Soc.*, 2001, **123**, 10699-10704.
53. C. L. Yueh, J. C. Jan, J. W. Chiou, W. F. Pong, M. H. Tsai, Y. K. Chang, Y. Y. Chen, Y. F. Lee, P. K. Tseng, S. L. Wei, C. Y. Wen, L. C. Chen and K. H. Chen, *Appl. Phys. Lett.*, 2001, **79**, 3179-3181.
54. J. G. Zhou, H. T. Fang, J. M. Maley, J. Y. P. Ko, M. Murphy, Y. Chu, R. Sammynaiken and T. K. Sham, *J. Phys. Chem. C*, 2009, **113**, 6114-6117.
55. Y. Liang, H. Wang, J. Zhou, Y. Li, J. Wang, T. Regier and H. Dai, *J. Am. Chem. Soc.*, 2012, **134**, 3517-3523.
56. J. R. I. Lee, R. W. Meulenberg, K. M. Hanif, H. Mattoussi, J. E. Klepeis, L. J. Terminello and T. van Buuren, *Phys. Rev. Lett.*, 2007, **98**, 146803.
57. J. T. Wright and R. W. Meulenberg, *Appl. Phys. Lett.*, 2012, **101**, 193104.
58. H. Y. Si, C. H. Liu, H. Xu, T. M. Wang and H. L. Zhang, *Nanoscale Research Letters*, 2009, **4**, 1146-1152.
59. J. V. Ortiz, *J. Chem. Phys.*, 1987, **86**, 308-312.
60. L. R. De Jesus, R. V. Dennis, S. W. Depner, C. Jaye, D. A. Fischer and S. Banerjee, *J. Phys. Chem. Lett.*, 2013, **4**, 3144-3151.
61. S. Banerjee, T. Hemraj-Benny, M. Balasubramanian, D. A. Fischer, J. A. Misewich and S. S. Wong, *ChemPhysChem*, 2004, **5**, 1416-1422.
62. V. Leon, R. Parret, R. Almairac, L. Alvarez, M. R. Babaa, B. P. Doyle, P. Ienny, P. Parent, A. Zahab and J. L. Bantignies, *Carbon*, 2012, **50**, 4987-4994.
63. R. M. Metzger, *Chem. Rev.,* 2003, **103**, 3803-3834.
64. S. Osswald, E. Flauhaut, H. Ye and Y. Gogotsi, *Chem. Phys. Lett.*, 2005, **402**, 422-427.
65. J. Gyeong Bok, M. Yoon, J. Park, M. Inhee and S. Joo-Hiuk, In 34th International Conference on Infrared, Millimeter, and Terahertz Waves, , Busan, Sept. 21-25, 2009; pp 1-2.
66. S. Campidelli, C. Sooambar, E. Lozano Diz, C. Ehli, D. M. Guldi and M. Prato, *J. Am. Chem. Soc.*, 2006, **128**, 12544-12552.
67. H. Kataura, Y. Kumazawa, Y. Maniwa, I. Umezu, S. Suzuki, Y. Ohtsuka and Y. Achiba, *Synth. Met.*, 1999, **103**, 2555-2558.
68. S. Bandow, G. Chen, G. U. Sumanasekera, R. Gupta, M. Yudasaka, S. Iijima and P. C. Eklund, *Phys.Rev. B*, 2002, **66**, 075416.
69. F. Villalpando-Paez, H. Son, D. Nezich, Y. P. Hsieh, J. Kong, Y. A. Kim, D. Shimamoto, H. Muramatsu, T. Hayashi, M. Endo, M. Terrones and M. S. Dresselhaus, *Nano Lett.*, 2008, **8**, 3879-3886.
70. A. Rahmani, J. L. Sauvajol, S. Rols and C. Benoit, *Phys. Rev. B*, 2002, **66**, 125404.
71. H. Rauf, T. Pichler, R. Pfeiffer, F. Simon, H. Kuzmany and V. N. Popov, *Phys. Rev. B*, 2006, **74**, 235419.
72. Y. F. Li, R. Hatakeyama, T. Kaneko, T. Izumida, T. Okada and T. Kato, *Nanotechnology*, 2006, **17**, 4143-4147.
73. L. Wang, J. Han, Y. Zhu, R. Zhou, C. Jaye, H. Liu, Z.-Q. Li, G. T. Taylor, D. A. Fischer, J. Appenzeller and S. S. Wong, *J. Phys. Chem. C*, 2015, **119**, 26327-26338.

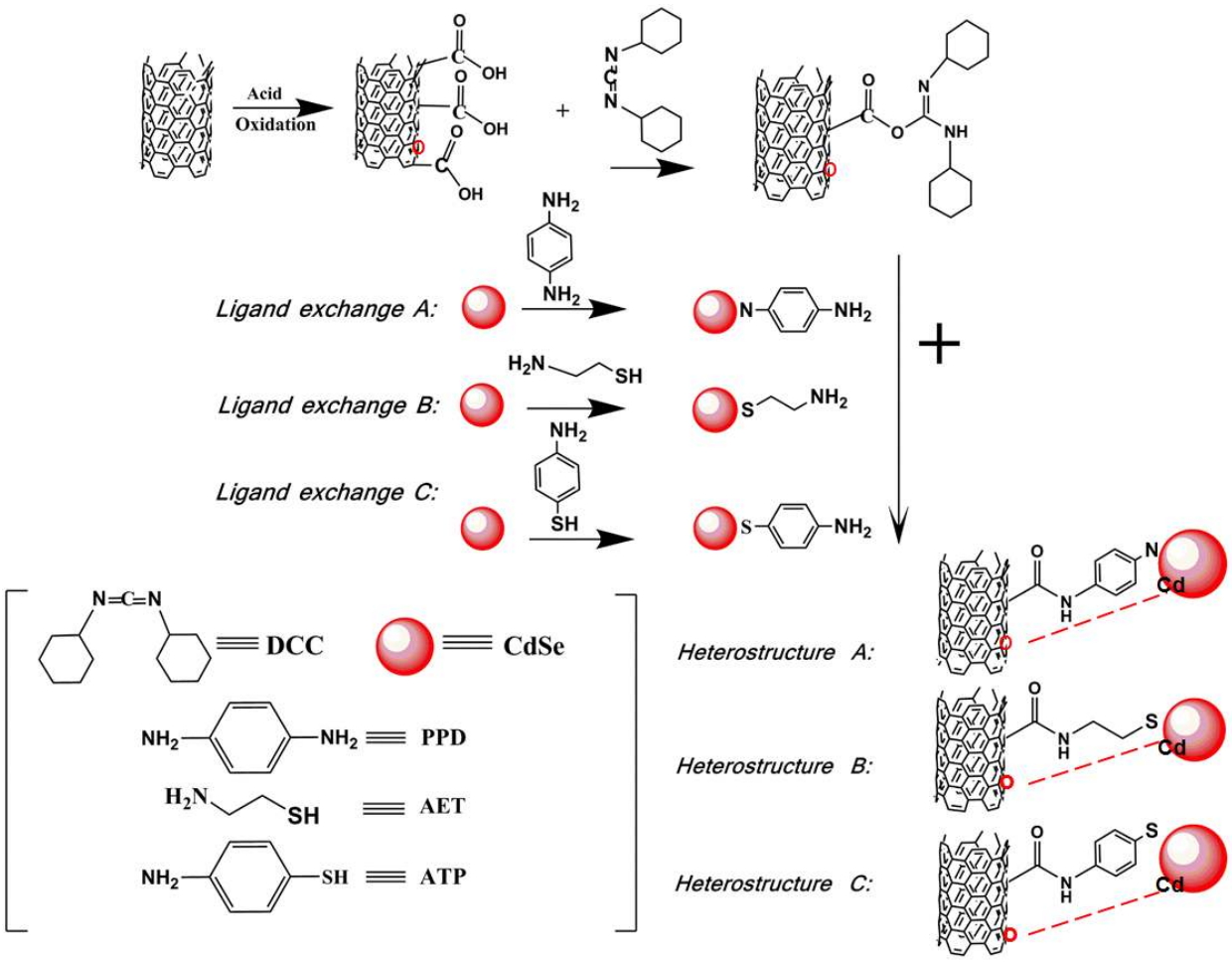

Scheme 1. Synthetic route associated with the attachment of DWNTs with CdSe QDs functionalized with PPD, AET, and PPD ligands, respectively.

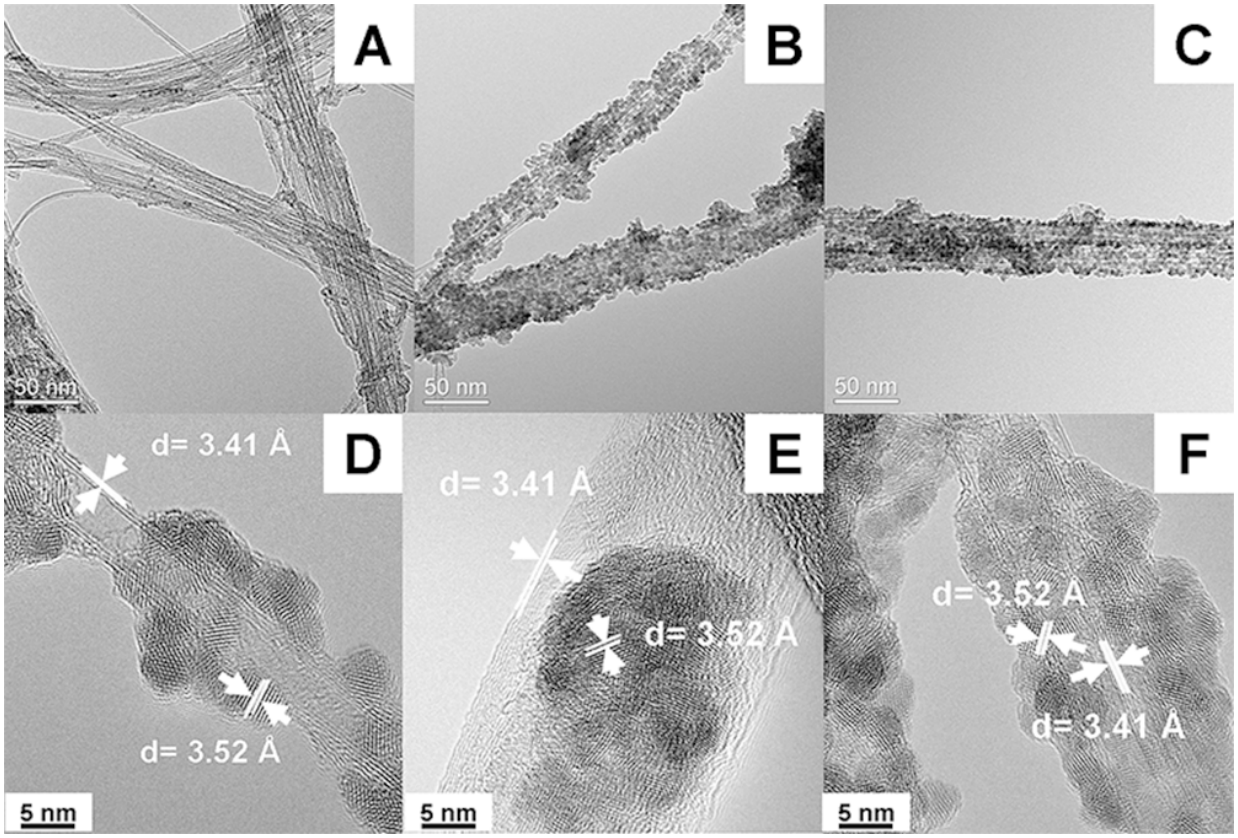

Figure 1. (**A, B, and C**)**.** TEM images and (**D, E, and F)** HRTEM images of DWNT-PPD-CdSe QD, DWNT-AET-CdSe QD, and DWNT-ATP-CdSe QD heterostructures, respectively, synthesized by an amide-mediated covalent attachment strategy.

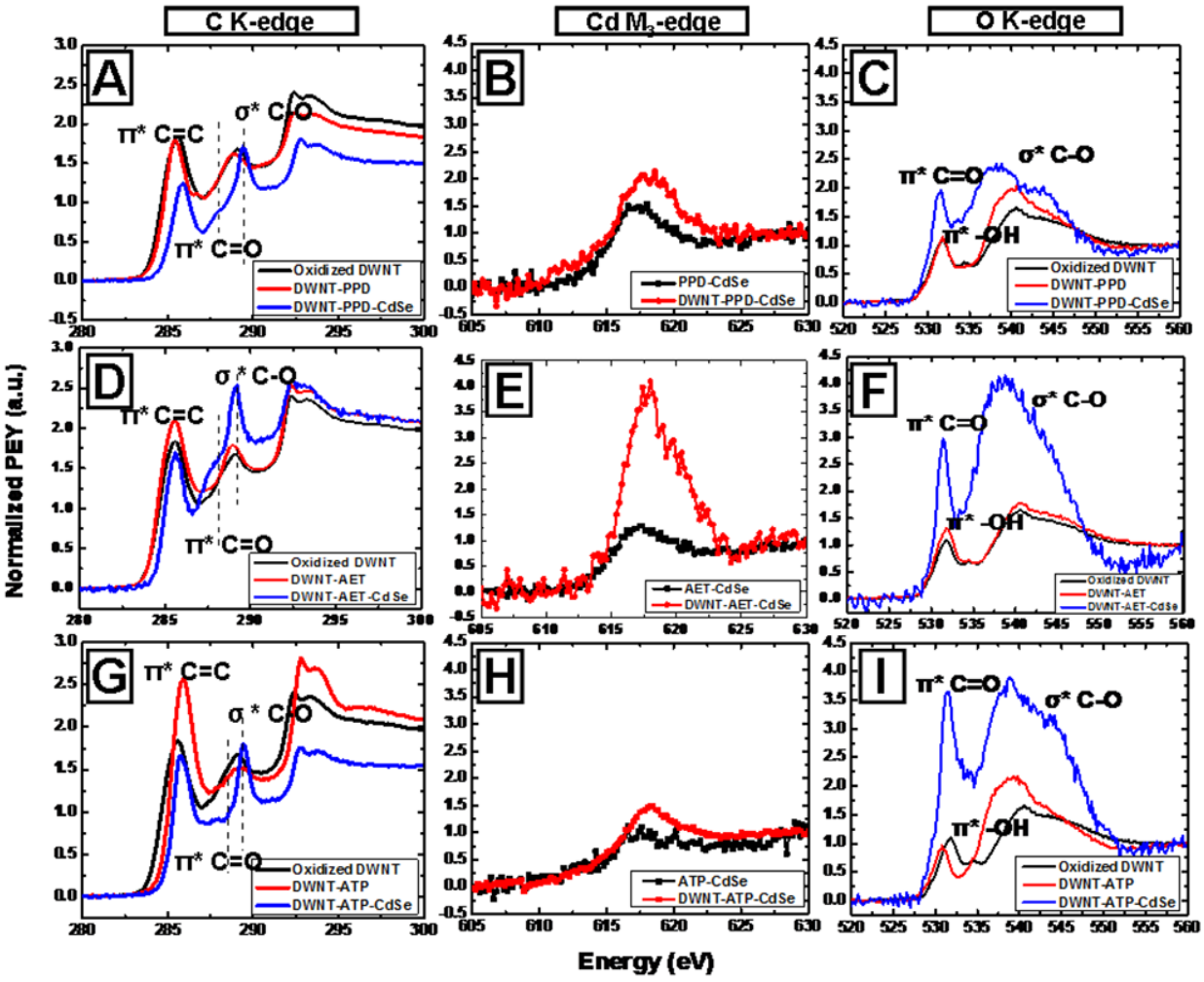

Figure 2. Probing the effect of varying ligands. Experimental (**A, D, and G)** C *K*-edge, (**B, E, and H**) Cd M_3-edge, and (**C, F, and I**) O *K*-edge spectra of DWNT-PPD-CdSe QD, DWNT-AET-CdSe QD, and DWNT-ATP-CdSe QD systems, respectively.

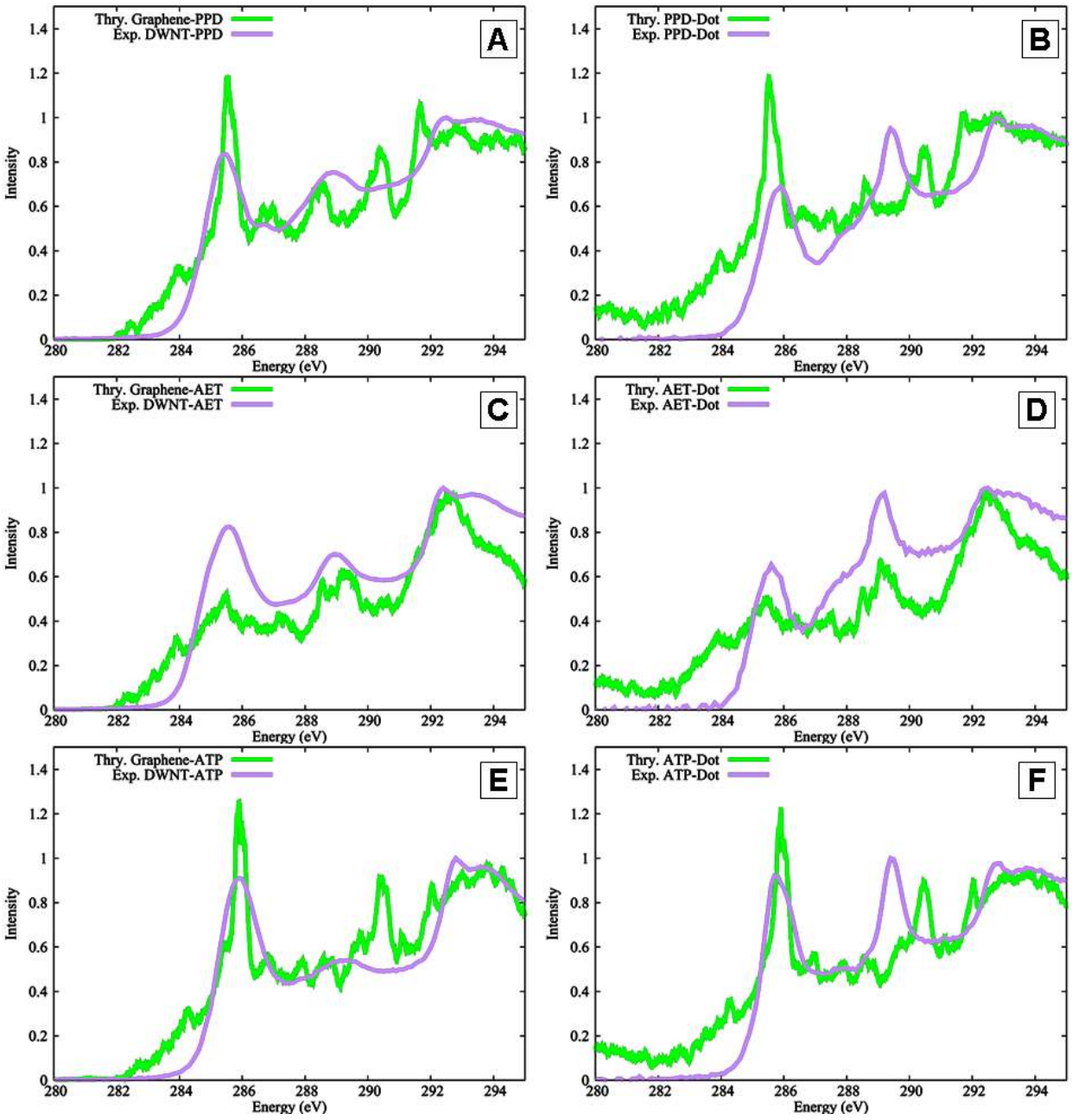

Figure 3. Comparisons of theoretically calculated versus experimental C *K*-edge NEXAFS spectra for the graphene-bound PPD/AET/ATP composites (**A, C, and E**), as well as for the graphene-bound PPD/AET/ATP-CdSe QD heterostructures (**B, D, and F**), respectively.

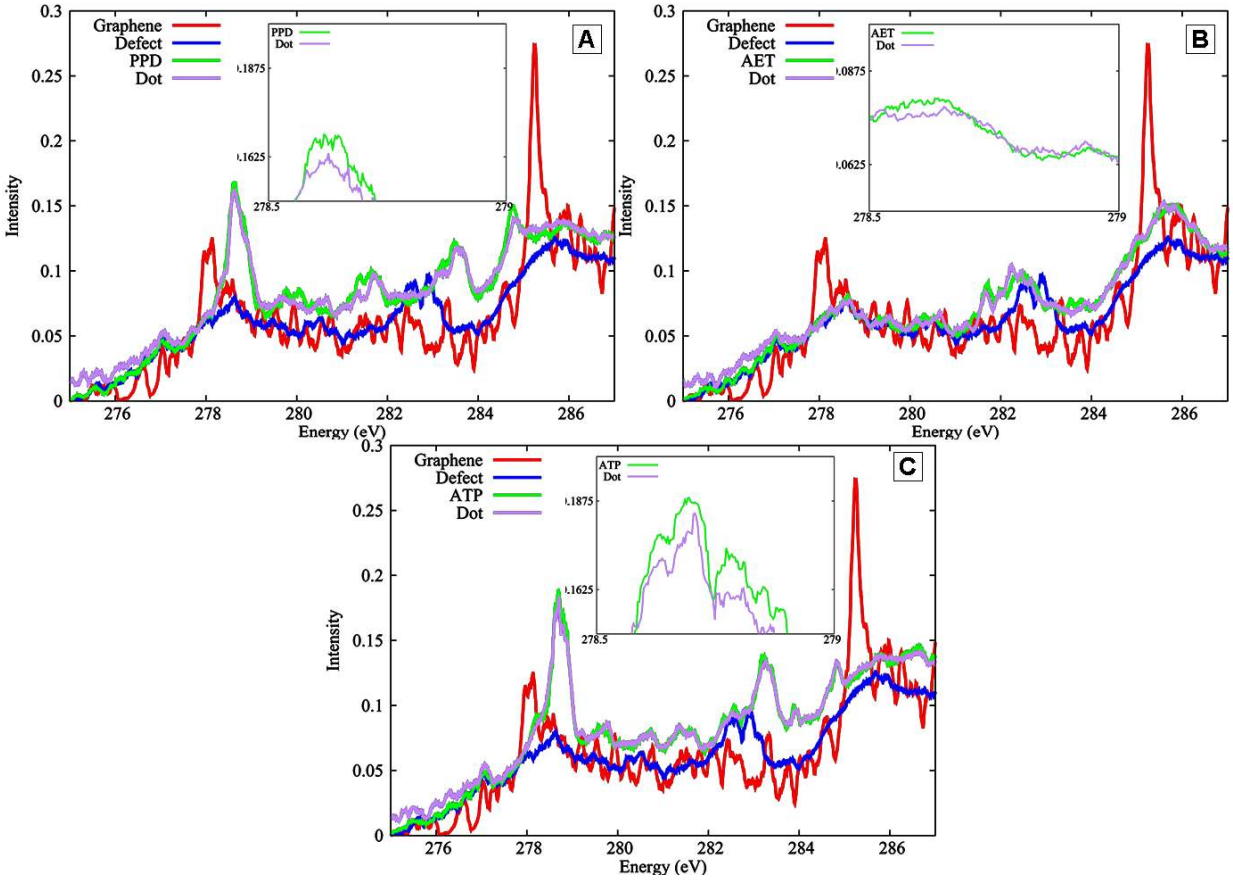

Figure 4. Theoretically calculated C *K*-edge NEXAFS spectra of pristine graphene (red), of defect-ridden (i.e. oxidized) graphene (blue), of various ligands bound to graphene (green), as well as of graphene-bound ligand-CdSe QD heterostructures (purple).

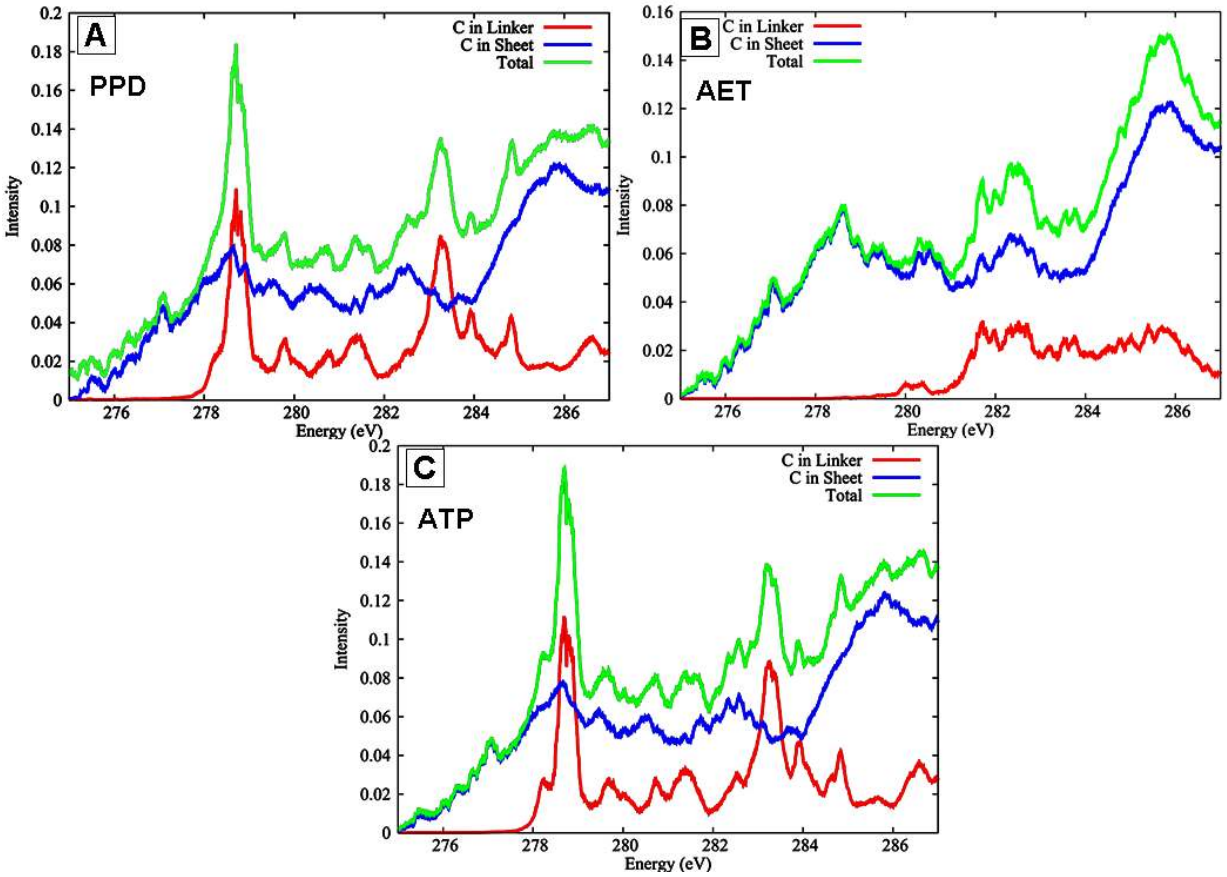

Figure 5. (A, B, and C). Breakdown of the NEXAFS spectra associated with graphene-bound PPD, AET, and ATP composites, respectively.

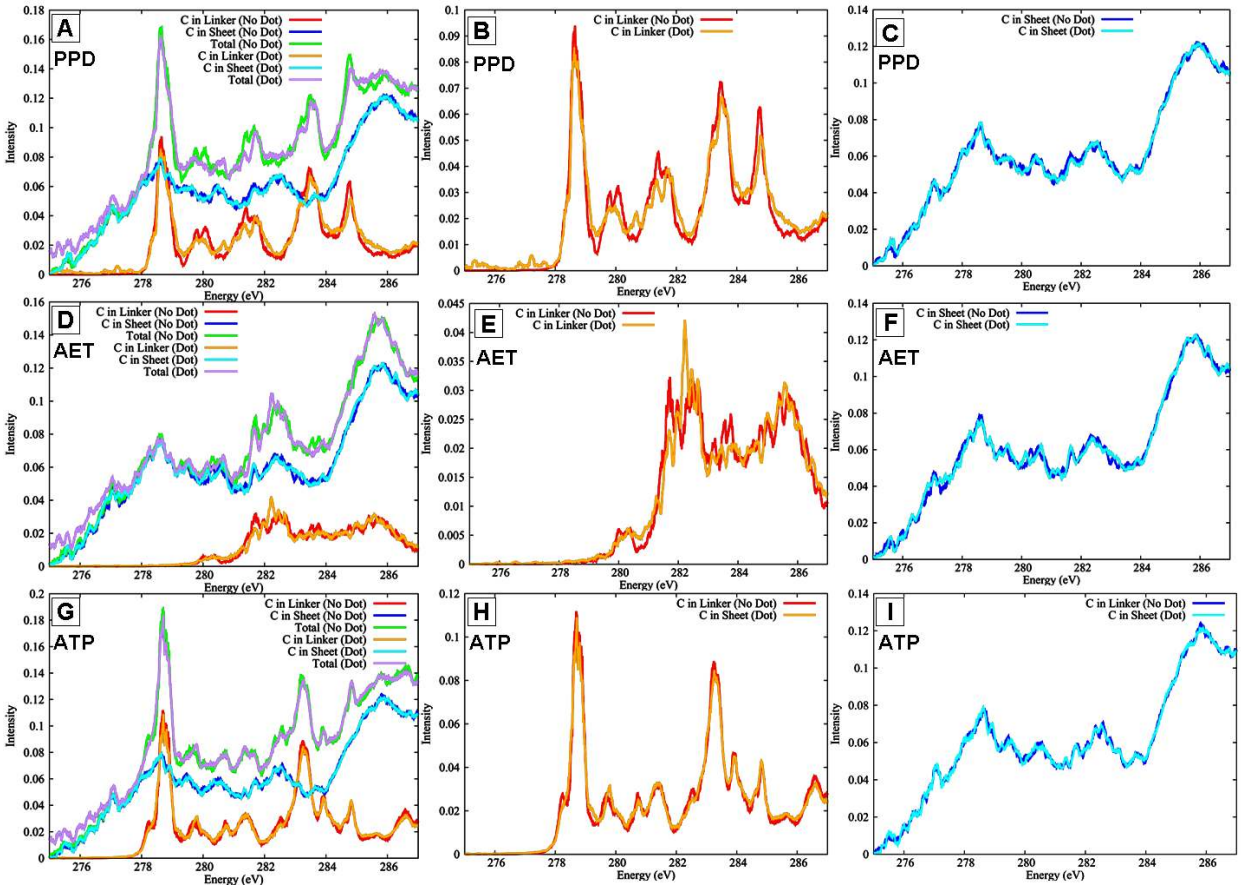

Figure 6. Differential carbon contributions to the C *K*-edge NEXAFS spectra associated with the graphene-bound PPD-QD heterostructures as compared with the graphene-bound PPD system (A-C), graphene-bound AET-QD heterostructures as compared with the graphene-bound AET system (D-F), and graphene-bound ATP-QD heterostructures as compared with graphene-bound ATP composites (G-I), respectively.

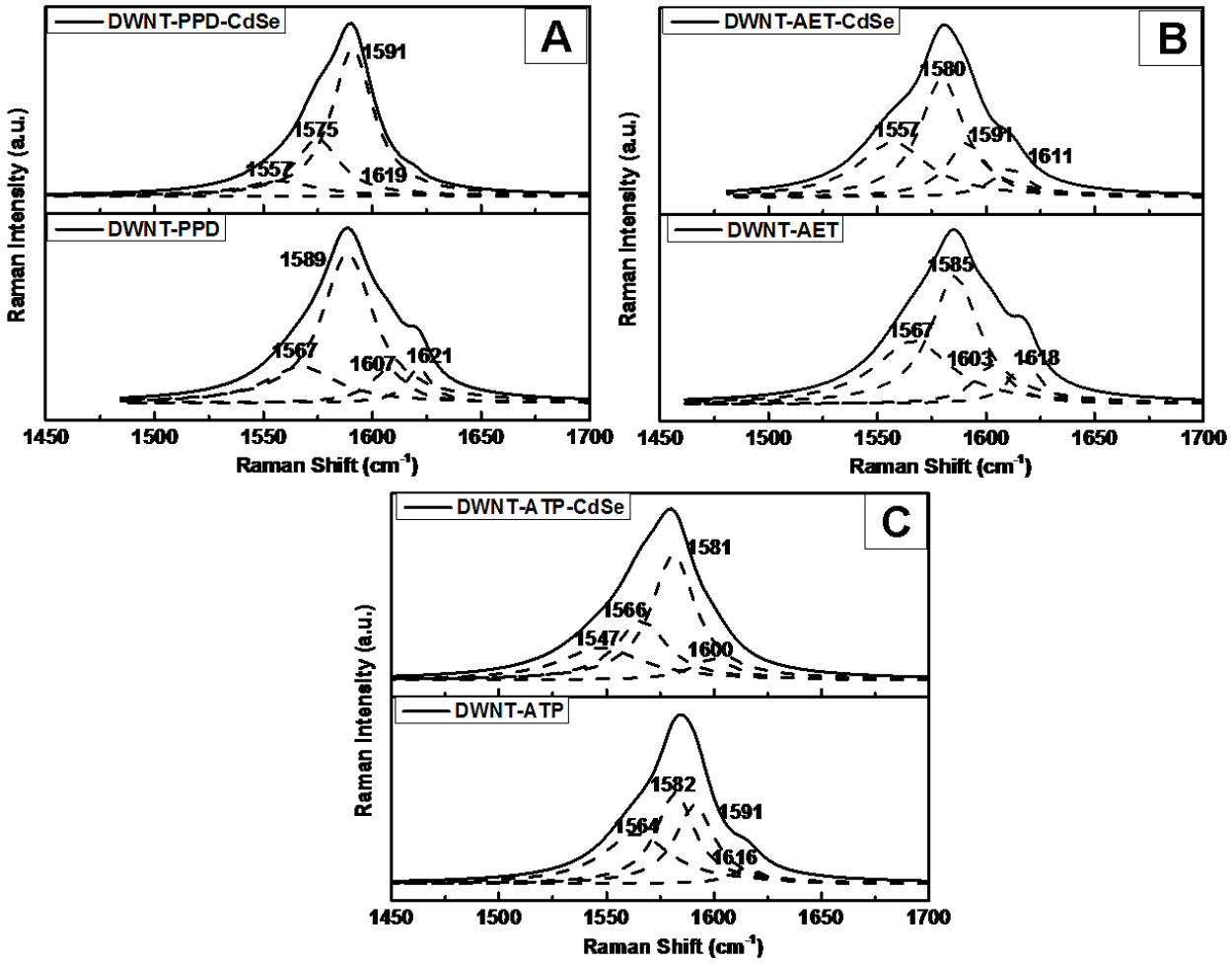

Figure 7. (A, B, and C). Raman G-band spectra, measured at an excitation wavelength of 514 nm (2.41 eV), of DWNT-PPD-CdSe QD, DWNT-AET-CdSe QD, and DWNT-ATP-CdSe QD heterostructures, respectively, by comparison with their respective controls. Reduced chi-square of the fitting is 3.2, 1.6, 2.7, 2.8, 1.3, and 1.7 for DWNT-PPD-CdSe QD, DWNT-PPD, DWNT-AET-CdSe QD, DWNT-AET, DWNT-ATP-CdSe QD, and DWNT-ATP structures, respectively.

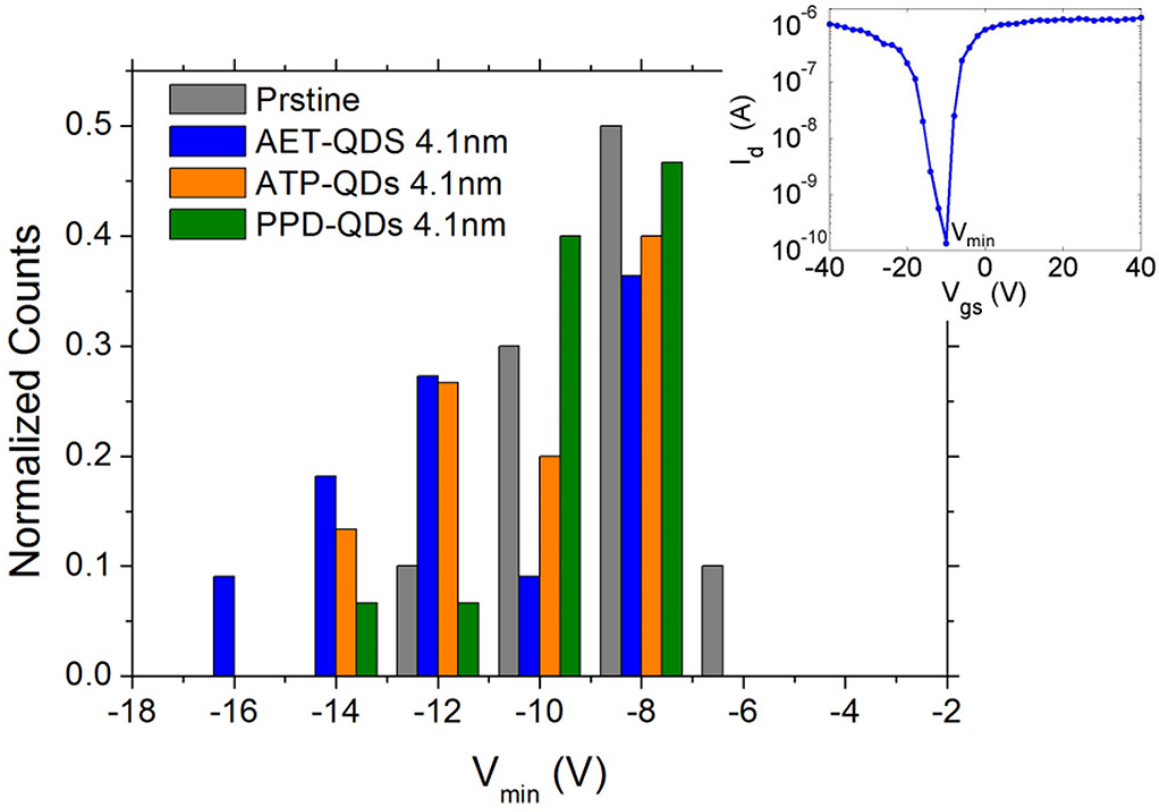

Figure 8. V_{gs} values, at which the current versus gate voltage characteristics of individual devices showed their minimum, for the various ligands tested. The inset shows a representative measurement for a device with ATP functionalization at a drain voltage of V_{ds} = -1 V. The channel length is 1 μm.

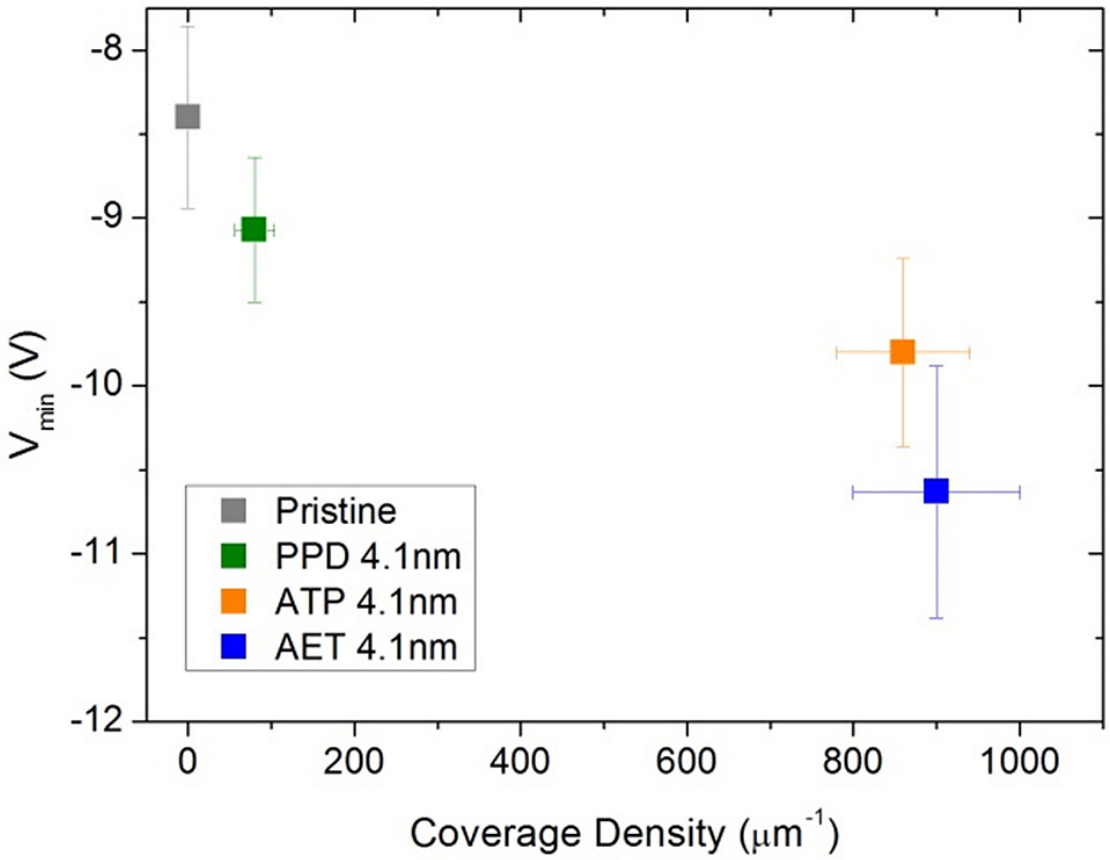

Figure 9. V_{min} vs. coverage density for various ligand-bound QD-CNT heterostructured samples.

Table 1. Summary of transport results for various functionalized ligand-QD CNT samples.

	PPD 4.1nm	ATP 4.1nm	AET 4.1nm
Shift of V_{min} [V]	-0.67±0.69	-1.4±0. 78	-2.23±0. 92
Coverage [μm^{-1}]	80±24	860±80	900±100

Table of Contents Figure:

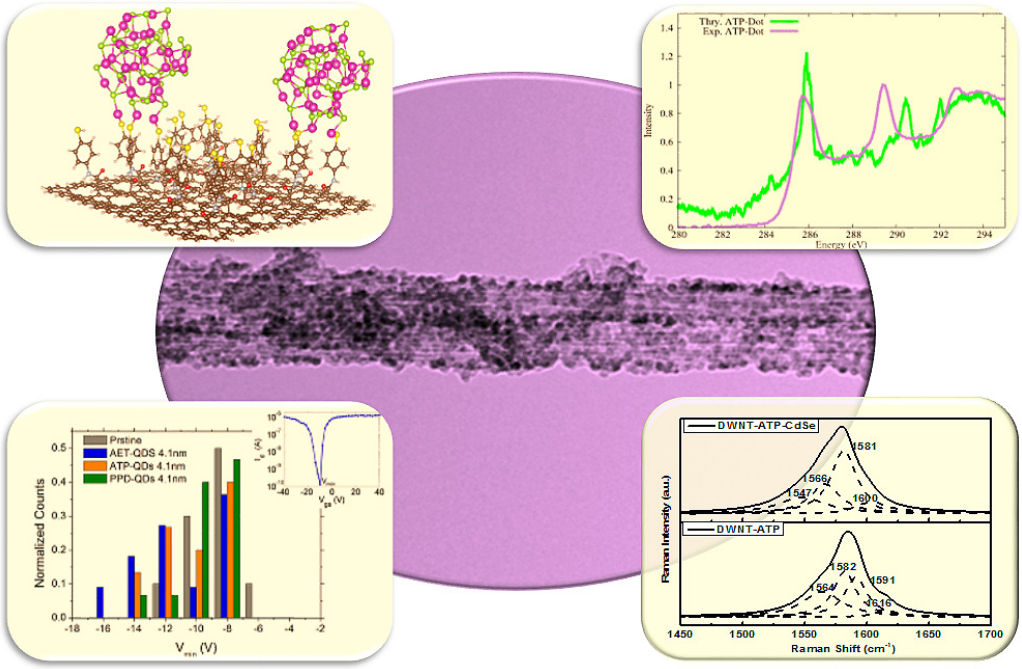

Table of contents entry: (maximum 20 words)
Probing the ligand-induced dependence of charge transfer within DWNT-CdSe heterostructures through complementary experimental and theory studies.